Probabilistic tractography for complex fiber orientations with automatic model selection

A tool to study structural connectivity in stroke patients

Edwin Versteeg

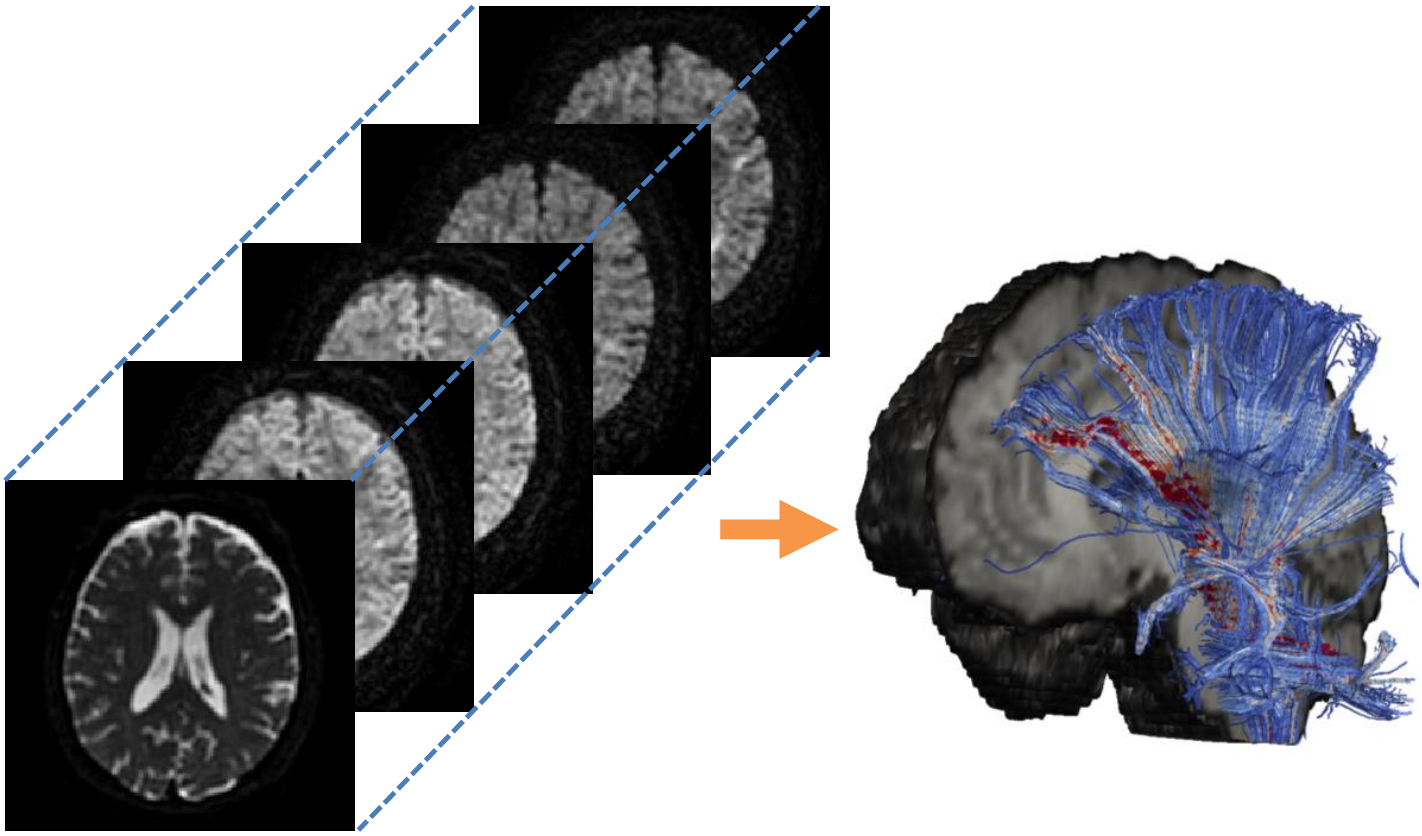

TU Delft

Probabilistic tractography for complex fiber orientations with automatic model selection

A tool to study structural connectivity in stroke patients

by

Edwin Versteeg

to obtain the degree of Master of Science
at the Delft University of Technology,
to be defended publicly on Wednesday August 16, 2017 at 14:00 PM.

Student number:	4228383	
Project duration:	December 6, 2016 – August 16, 2017	
Thesis committee:	Dr. F.M. Vos,	TU Delft & AMC, supervisor
	Ir. O. Filatova,	TU Delft, supervisor
	Dr. Ir. W. Mugge,	TU Delft
	Prof. Dr. Ir. L.J. van Vliet,	TU Delft

An electronic version of this thesis is available at `http://repository.tudelft.nl/`.

TU Delft

Abstract

Stroke is one of the leading causes of both death and disability in the world. Consequently, the processes underlying motor recovery are a hot research topic. Electroencephalography (EEG) and diffusion weighted magnetic resonance imaging (dMRI) are two modalities that can be used to find functional and structural predictors for this motor recovery, respectively. Specifically, EEG measures the sources of activity (dipoles) in the brain while dMRI provides estimates of the properties of white matter (WM) tracts such as the fiber orientation. The estimated fiber orientations can be used to reconstruct WM connections in the brain by performing fiber tractography.

In this thesis, we aim to introduce a framework for model selection and probabilistic tractography with parsimonious model selection. Practically, we use a range of multi-tensor models to cope with regions with multiple fiber populations. Furthermore, our probabilistic tractography uses the Cramér-Rao lower bound to capture the uncertainty in the fiber orientations. We mitigate the effect of overfitting by using a model selection method that incorporates the ICOMP-TKLD criterion to determine the most appropriate tensor model in each voxel. Ultimately, this framework can be applied to data from stroke patients and combined with functional regions obtained from EEG.

We assessed the performance of the model selection method by investigating the influence of b-value and noise on the ability to detect crossing fibers in the fibercup phantom and human data. In the phantom, our model selection reconstructed all the crossings for the b-value combination of 1500 and 2000 s/mm^2 and at a signal-to-noise-ratio (SNR) comparable to clinical acquisitions. Moreover, our model selection method was able to identify the crossing of the corpus callosum and corticospinal tract in the human data.

A range of step sizes and curvature thresholds was used to investigate the sensitivity of our tractography to its input parameters. In general, a smaller step size and lower curvature thresholds resulted in more deterministic behavior, while a larger step sizes and higher curvature thresholds led to more probabilistic behavior and deeper propagation into the gray matter in human data.

We compared the performance of our framework and the open source diffusion MRI toolkit Camino on the fibercup phantom and healthy control data. In this comparison, our framework performed better in curved bundles and reconstructed more lateral projections of the corpus callosum.

Lastly, we explored the subdivision of the brain into modules for stroke patients and healthy controls, by combining our framework with sources obtained from EEG. Fewer modules were found in the patient group, which might be attributed to a change in structural connections after stroke.

Altogether, we have shown that our framework was able to select the appropriate diffusion models in crossing fiber regions and track across these crossings both in a phantom and human data. Furthermore, we demonstrated that it is feasible to combine our framework with source locations obtained from EEG.

Acknowledgments

First of all, I would like to thank Lena Filatova and Frans Vos for their supervision and valuable input to my thesis. Furthermore, I would like to thank everyone in the Quantitative Imaging group for their friendliness, weirdness and table soccer during the breaks. Specifically, I would like to thank the people from the master room (Joost, Aloys, Ellen and Sten) for the interesting conversations and bad jokes. Lastly, a special thanks to Lovisa Westlund Gotby for supporting me both in my thesis and at home.

Edwin Versteeg, August 2017

Contents

1 Introduction

Stroke is one of the leading causes of both death and disability, as well as one of the main causes for a decreased quality of life in the world [1, 2]. Particularly, the recovery of motor function after stroke is an important factor for the qualify of life of a patient [3]. A possible biomarker for predicting this recovery exists in the form of the functional and structural integrity of the ipsilesional corticomotor tract [3, 4].

Two modalities that can aid in predicting stroke recovery are electroencephalography (EEG) and diffusion weighted magnetic resonance imaging (dMRI). EEG provides functional information by measuring the sources of brain activity [5], while dMRI gives structural information by delineating and characterizing white matter (WM) bundles [4]. Specifically, dMRI measures the diffusion of water in the WM bundles. Diffusion models are fitted to the data to estimate properties of WM tracts related to, e.g., the fiber orientation, and fiber density [6, 7]. Probabilistic fiber tractography algorithms strive to reconstruct WM connections in the brain by following these fiber orientations whilst taking the noise in the data into account [8]. However, the amount of fiber orientations present is not constant over the brain, hence some type of model selections is needed to assure an accurate reconstruction of the WM connections [9].

The aim of this thesis is to introduce a framework for model selection and probabilistic tractography with parsimonious model selection. Essentially, our approach takes uncertainties into account that are derived directly from the model fitting procedure. To achieve this we apply multi-tensor models, which model the signal as a combination of multiple fiber compartments and an isotropic compartment. Additionally, this framework can be applied to data from stroke patients and combined with functional regions obtained from EEG.

In this thesis, we will asses the performance of the different components of this framework. First of all, the model selection will be assessed by investigating the influence of b-value, noise and parametrization on the ability to detect crossing fibers. Furthermore, we will perform a sensitivity analysis of the tractography to investigate the effect of step size and curvature threshold on the outcome. Additionally, our framework will be compared to an off-the-shelf dMRI toolkit in the form of Camino [10], which can perform both model selection and probabilistic tractography. Lastly, our framework will be combined with dipole locations obtained using EEG to test the feasibility of using our framework to compare biomarkers between patients affected by stroke and a control group.

2

Literature

2.1. Stroke and stroke recovery

Stroke occurs when the blood flow to certain brain areas is severely limited and is caused by either the occlusion of a cerebral artery by a blood clot (ischemic stroke), or compression of brain tissue due to a bleeding (hemorrhagic stroke) [11]. Both causes are visualized in Figure 2.1. As a consequence of the decreased blood flow, brain cells are deprived of oxygen, which leads to cell death. The resulting damage to the brain can result in death of the patient or, when the patient survives, partial loss of brain functions which can lead to decreased functionality of the limbs and problems with producing and processing speech. Furthermore, the severity and extend of function loss depends on the position of the stroke in the brain and the amount of brain damage [11].

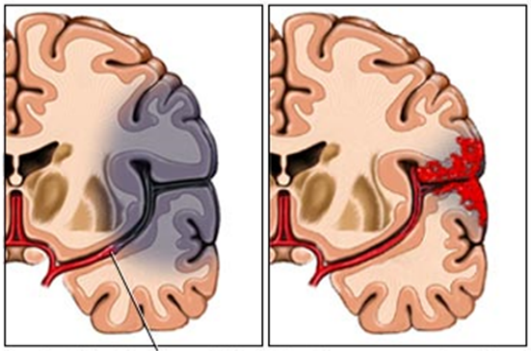

(a) Ischemic stroke (b) Hemorrhagic stroke

Figure 2.1: Schematic representations of ischemic and hemorrhagic stroke, adapted from [12]

The remaining level of disability of stroke patients is determined by the recovery process after stroke and is a major factor in their quality of life [13]. The recovery process consists of re-learning the lost motor functions through physical therapy and a spontaneous element of which the origin is not precisely known [3]. A better understanding of the underlying biological mechanisms governing these two processes could aid in improving the outcome of the rehabilitation process and consequently the quality of life of stroke patients [14].

2.2. The brain and diffusion

The brain can roughly be split up into two different tissue types: gray matter and white matter. The gray matter (GM) contains neuronal cell bodies and dendrites, and can be found in the cerebral cortex and basal nuclei. Moreover, gray matter is predominantly found in the functional regions of the brain, such as the sensory, motor and association areas. White matter (WM) mainly consists of myelinated fibers, the axons, that are grouped into WM bundles/tracts. Specifically, the WM bundles form the connections that allow the different functional regions of the brain to communicate with each other and the rest of the body [11].

2.2.1. Diffusion in the brain

Diffusion is the random motion of molecules, such as water, due to their thermal energy. Importantly, isotropic diffusion occurs when the motion of the molecules is equal in all directions, whereas a directionally dependent diffusion is referred to as anisotropic diffusion [15]. In the brain, anisotropic diffusion primarily occurs in the white matter, whereas the diffusion in gray matter is mostly isotropic.

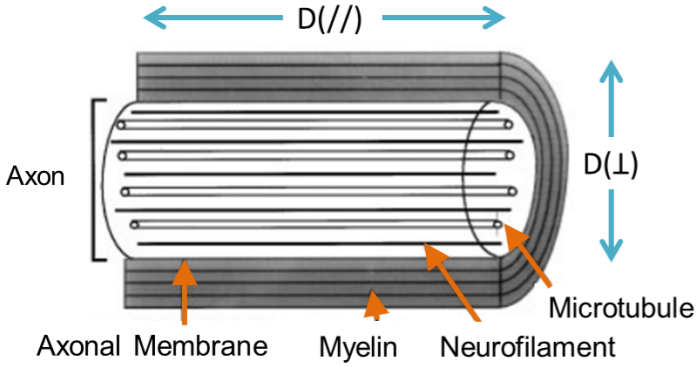

Figure 2.2: Schematic drawing of the diffusion in an axon, adapted from [16]

The axonal cell membranes are the dominant component in the diffusion in and around axons in the white matter (see Figure 2.2). These membranes limit the diffusion of water in the radial direction (D(⊥)), while the water can move freely along the axial direction (D(//)). Other cellular components such as the myelin sheath, neurofilaments and microtubules also influence the degree of anisotropy as these impede the radial diffusion [16].

2.3. MRI basics

In magnetic resonance imaging (MRI), magnetic fields are used to manipulate and measure the magnetization due to nuclear spins in the body. In order to create an image, three types of magnetic fields are used in MRI. First of all, the nuclear spins are aligned in the direction of a strong static magnetic field (> 1.5 Tesla), the B_0 field. The nuclear spins (and therefore the magnetization) will start to precess around this B_0 field at a frequency known as the Larmor frequency, which is proportional to the field strength.

Gradient coils are used to generate gradients in the static magnetic field and introduce a positional dependency of the precession frequencies, which makes it possible to differentiate between signals coming from different positions in the body. Lastly, radio frequency (RF) fields are used to flip the magnetization into a plane that is transverse to the B_0 field. This allows for measurement of the weak RF fields generated by the precessing spins using receive coils. As a result of the positional dependence of the precession frequency this signal can be used to form an image [17].

2.4. Diffusion weighted MRI

The first description of the effect of diffusion on the relaxation time of spins, the shortening of the T_2 relaxation, was given by Carr and Purcell in 1954 [18]. In 1965, Stejskal and Tanner developed a sequence of gradient pulses (Figure 4.12) to explicitly weigh the magnetic resonance (MR) signal with diffusion [19], which formed the basis for the introduction of dMRI in the 1980s [20].

A typical diffusion sensitizing pulse sequence introduces a positional dependency of the spin precession frequency by applying two gradients seperated by a rephasing 180^o-pulse. Importantly, this switching of gradients has no net effect in the case of a stationary spin, as the accumulated phase during the first gradient is compensated by the second gradient. However, spins that move in the direction of the gradient will have a residual phase due to different magnetic fields felt by the spins during the two gradient pulses. This difference in phase results in attenuation of the measured MR signal [21]. Other pulse sequences are also able to sensitize the MR signal to diffusion. For example, the same effect can be obtained by removing the 180^o-pulse and reversing the polarization of the second gradient pulse, which is known as a bipolar gradient [15].

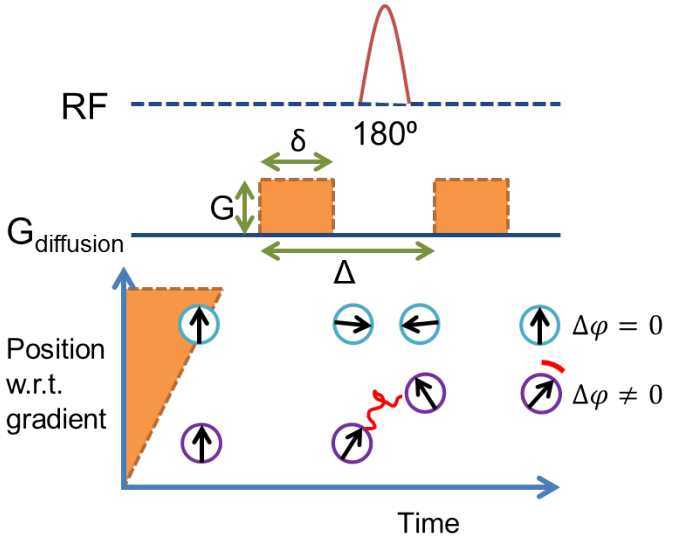

Figure 2.3: Schematical representation of the positional dependency of precession frequency during the bipolar gradients. Based on [21].

2.4.1. The diffusion signal

The MR signal in dMRI is proportional to the T_2 relaxation, the diffusion in a voxel and the intra-voxel incoherent motion. These last two parameters cannot be measured independently and are combined in the apparent diffusion coefficient (ADC) [22], which results in the signal equation given below:

$$S = [\rho]e^{-t/T_2}e^{-bD}. \tag{2.1}$$

Equation 2.1 shows that the signal measured in dMRI is proportional to the proton density $[\rho]$ and can be seen as a mix of a T_2 weighted signal and a diffusion weighted signal. The first exponential represents the T_2 weighting which depends on t the echo time and the T_2 relaxation constant. The second exponential, which denotes the diffusion weighting, depends on the diffusion weighting factor b (b-value) and the apparent diffusion coefficient D [17].

Importantly, the axons in the brain have a size in the order of micrometers while the resolution of dMRI is in the order of millimetres. Hence, the signal from one voxel in a dMRI acquisition measures a bulk effect of e.g. multiple fiber bundles and other extra cellular components, and not the diffusion in individual axons [23].

The b-value is a function of the parameters shaping the gradient pulses (see Figure 4.12), has units of $mm^{-2}s$ and is defined as:

$$b = \gamma^2 G^2 \delta^2 (\Delta - \delta/3). \tag{2.2}$$

where γ represents the gyromagnetic ratio, G denotes the strength of the diffusion sensitizing gradient pulses, δ is the duration of the separate pulses and Δ stands the time between the starting points of the two pulses [22]. Moreover, it determines the sensitivity of the MR acquisition to diffusion. In particular, a higher b-value will allow for the measurement of smaller ADC values, but also decreases the signal-to-noise ratio (SNR) of the acquisition, as the signal produced by voxels with a large ADC will be below the noise floor [24].

2.5. Diffusion tensor MRI

In vivo, the exponential proportionality of the dMRI signal to a single scalar ADC is only true in tissue with isotropic diffusion. If we want to describe anisotropic diffusion, such as in WM bundles, the 3D diffusion profile needs to be taken into account [25]. The diffusion tensor (DT) models the diffusion profile as an ellipsoid by assuming a single Gaussian diffusion process in a voxel, which is described by a 3 x 3 DT [6]:

$$\mathbf{D} = \begin{bmatrix} D_{xx} & D_{xy} & D_{xz} \\ D_{yx} & D_{yy} & D_{yz} \\ D_{zx} & D_{zy} & D_{zz} \end{bmatrix} \tag{2.3}$$

with the diagonal elements representing the diffusion in three orthogonal directions and the off-diagonal elements representing the correlations. In general, the orthogonal directions (x,y,z) are aligned with the gra-

dients of the MR-system [20]. The DT can be estimated by solving a linear system of 7 acquisitions, which consist of 6 acquisitions with non-colinear gradient directions and a b=0 acquisition to estimate the non-diffusion weighted signal [26].

The eigenvectors and eigenvalues of the DT are used to probe the microstructure of tissue in a voxel. Particularly, the first eigenvector defines the orientation of the fiber bundles while the eigenvalues can be used to describe the microstructure using rotationally invariant measures such as the degree of anisotropy (fractional anisotropy or FA) and mean diffusivity (MD) [27]. These are defined as:

$$\mathrm{FA} = \sqrt{\frac{1}{2}}\frac{\sqrt{(\lambda_1-\lambda_2)^2+(\lambda_2-\lambda_3)^2+(\lambda_3-\lambda_1)^2}}{\sqrt{\lambda_1^2+\lambda_2^2+\lambda_3^2}}; \quad \mathrm{MD} = \frac{(\lambda_1+\lambda_2+\lambda_3)}{3}, \tag{2.4}$$

where λ_i denotes the i$^{\text{th}}$ eigenvector of the DT.

The main applications of DTI are in the field of neurology where the fiber orientations, by reconstructing WM pathways using fiber tractography, can be used as an aid in the resectioning of brain tumors [28] or as a predictive tool in stroke patients [29]. Furthermore, the scalar measures can be used to investigate the progress of diseases such as multiple sclerosis, Parkinson's disease, Alzheimer's disease and autism, and the effects of education and aging on the brain [30]. Additionally, other applications exist in quantifiying multiple sclerosis in the spinal cord [31], imaging muscle tissue (e.g. the tongue) [32], and planning and assessing treatments in radiotherapy [33].

2.5.1. Limitations

DTI and its assumption of a single Gaussian process has severe limitations as it is well known that the single tensor model does not hold in voxels with non-Gaussian diffusion [34]. This is the case in voxels with multiple fiber populations, whose prevalence has been estimated to range from 33% up to ~90% of the WM voxels [9, 35]. Consequently, DTI based tractography leads to erroneously reconstructed WM pathways [36], and ambiguous correlations of the scalar measures [37]. For example, in the case of two crossing fibers an increase in the FA of one fiber population will result in a decrease in the FA measured using DTI [38].

2.6. Advanced diffusion models

Several methods have been developed to address the issue of multiple fiber populations in a voxel. These can be subdivided into methods that estimate the spin displacement probability [39–41] or model the signal coming from different fiber compartments [9, 34, 42–45]. The data acquisition for these methods uses a larger number of gradients by uniformly distributing gradient directions at 1 b-value (High angular resolution diffusion imaging or HARDI) [34], or by sampling the space of diffusion weighings b (q-space) in some other fashion [40].

2.6.1. Q-space based

Q-space based methods use the signal measured in q-space and its relation to the spatial distribution of the spins via a Fourier transform. A large number of points in q-space is necessary for reconstructing the 3D diffusion profile leading to long scan times [39]. However, fewer points can be used when assuming a certain distribution of spin displacement or the signal in q-space which is used in methods such as Q-ball imaging and persistent angular structure (PAS) MRI [40, 41]. The main application of these methods is as a model-free method to estimate fiber orientations, which can derived from the peaks of the 3D diffusion profile, and perform fiber tractography [46].

2.6.2. Mixture models

Mixture models model the signal from multiple fiber populations as a combination of different fiber bundles and extra-axonal compartments. A general signal model for these methods can be defined as:

$$S = (1-f)\left(\sum_i v_i S_{fiber,i}\right) + f S_{extra-axonal}, \tag{2.5}$$

where S_{fiber} and $S_{extra-axonal}$ denote the signal arising from the fiber and extra-axonal compartments, f stands for the volume fraction of the extra-axonal compartment and v_i represents the volume fraction of each fiber compartment.

Different approaches for splitting the signal exist, such as modelling the signal as a combination of hindered (Gaussian) diffusion outside the axons and restricted (non-Gaussian) diffusion inside the axon (CHARMED) [42], separating the signal into intra-cellular, extra-cellular and ceribrospinal fluid (CSF) compartments (NODDI) [45], extending the DT formalism with multiple anisotropic tensors and one isotropic tensor (Multitensor models) [43, 47], and modelling the signal as a convolution between a diffusion dependent signal response function and a fiber orientation density function (spherical deconvolution) [48].

Importantly, the mixture models do not only include information about the fiber orientations but can also provide scalar quantities characterizing the microstructure of the brain [23]. Scalar quantities estimated in these models range from the volume fractions of the intra and extra axonal components (NODDI, CHARMED, Multitensor models) [49], the dispersion of axons (NODDI) [45], the FA for separate compartments (Multitensor models) [24], and other FA-like measures (Spherical deconvolution) [40, 50].

2.7. Model selection

The aforementioned mixture models are capable of modelling the non-Gaussian diffusion signals produced by multiple fiber populations. However, applying these models in voxels with a single fiber population may result in overfitting and thus erroneous estimations of fiber orientations and model parameters [51].

In practice, model selection is used to either provide an a-priori estimate of the fiber populations or match the suitable model to the data. Different model selection approaches exist that aim to select the model parameters best supported by the data [9] (Automatic relevance determination), estimate the number of fiber compartments [35], determine the type of diffusion [52], and find a trade-off between goodness of fit and model complexity [53] (parsimonious model selection).

All these different model selection methods have their own limitations. For example, the process of automatic relevance determination is very time consuming due to its use of Markov Chain Monte Carlo sampling [9]. Furthermore, data specific thresholds are needed for the methods that estimate the number of fiber compartments and determine the type of diffusion [35, 52]. Lastly, parsimonious model selection methods require all the models to be fitted to the data separately, thus take more time depending on the amount of models used [9, 53].

2.8. Fiber tractography

Most fiber tractography algorithms strive to reconstruct WM connections in the brain by following the local tract orientations that were estimated using the aforementioned methods. Furthermore, other (global) tractography algorithms exist that aim to find the total configuration of WM bundles based on the dMRI-data [54, 55]. The rest of this section will focus on local tractography algorithms because of their relevance to the scope of this thesis.

Tractography algorithms can be roughly subdivided into two types: deterministic and probabilistic. Deterministic algorithms use line propagation techniques to generate streamlines from a seed region [56]. However, noise in the dMRI acquisition can introduce uncertainties and possible errors in the generated streamlines [57]. Alternatively, probabilistic tractography algorithms target to address this issue by modelling a probability density function (PDF) of the fiber orientations [8]. A density of streamlines can be obtained by sampling this PDF, which is assumed to relate to the probability of connection between voxels.

Current methods to estimate the fiber orientation PDFs are based on the shape of the diffusion tensor [58], the variability between acquisitions (i.e. bootstrap methods) [37, 59], and the posterior probability of tensor parameters (Bayesian inference) [8]. Limitations of these methods include the increased scanning time [60] and long calculation times for Bayesian inference methods [61].

2.8.1. Parameters of tractography

In general, the behavior of a tractography algorithm depends on its propagation method, stopping criteria, use of prior knowledge and selection of seed points. The propagation method influences the ability to follow curved trajectories and track across crossings. In these regions a too large or constrained step size might result in an overshoot. Interpolating the estimated fiber directions or adapting the step size and direction based on local curvature are among the methods developed to mitigate this overshoot [62].

Stopping criteria define the endings of the streamlines and can be based on an anisotropy threshold [62], maximum allowed curvature [8], and/or regional mask. The aim of these criteria is to either prevent tracking in regions where the estimated fiber orientations are ill-posed (gray matter), or prevent implausible streamlines with sharp curvature. Additionally, prior knowledge can be used as an extra filter in the form of ROIs

(waypoints) that a streamline should pass through to be considered anatomically plausible [63, 64].

Finally, the results of tractography algorithms, in particular deterministic algorithms, are sensitive to their starting point. The placement of seed points can be done manually, e.g. based on prior knowledge about anatomical relevance, and automatically based on either an anatomical atlas [65], or activation maps from functional-MRI (fMRI) [66, 67] and electroencephalography (EEG) [68]. However, automatic methods for seed placement are preferred as they result in better reproducibility of the tractography [69].

2.9. Basic principles of EEG

During activity, individual neurons in the brain produce intracellular and extracellular electric fields [70]. The electric fields produced by pyramidal cells, which are located in the cortex, are of particular interest in EEG, see Figure 2.4. These pyramidal cells consist of long dendrites extending through the cortex and produce a net potential, the so-called open local field, which can be represented by a dipole source with a certain strength, position and direction. This potential difference can be measured in EEG by placing a number of electrodes on the scalp [71].

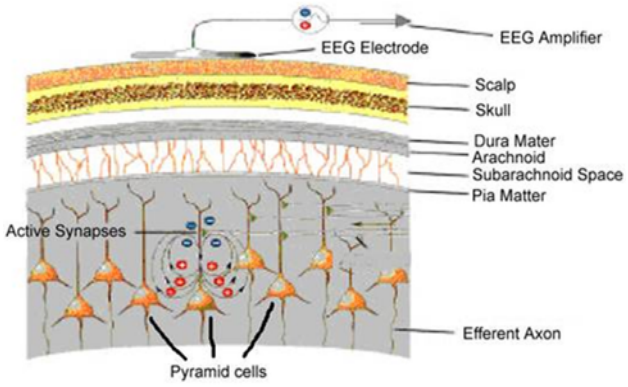

Figure 2.4: Schematic representation of an EEG measurement and the underlying anatomy, adapted from [12]

Notably, the 2D scalp field measured does not uniquely map to one 3D configuration of dipoles. In other words, there will be an infinite number of valid dipole configurations for one scalp field map, which is known as the inverse problem. The main challenge in EEG is to find approaches that solve this inverse problem and unmix the 2D scalp field into the different dipole sources [70].

Evidently, several assumptions have to be made for the distribution and origin of brain activity during different mental processes to allow for unmixing of the EEG signal. In practice, such approaches are either based on experimental inference or modelling of the sources. Experimental inference methods intend to unmix the EEG signal based on the additivity of electric fields in the brain. The difference in scalp field between an experimental task and a resting state or another reference task is assumed to only relate to sources specific to the experimental task [70].

Model based unmixing assumes either a specific time behavior of the EEG signal (Temporal models) or a certain spatial distribution of the sources (Spatial models). Examples of temporal models are independent component analysis (ICA) [72] and cluster analysis [73], which assume that the EEG signal is composed of a series of components with independent temporal behavior or a sequence of briefly stable microstates, respectively. Lastly, the spatial models can be subdivided into discrete and distributed solutions that assume either a small number of strong sources or a large number of distributed weak sources [70].

2.10. Application of EEG and MRI in stroke

As mentioned before, motor recovery is an important factor in the quality of life of a patient after stroke that can be studied using EEG and dMRI. A possible predictor for motor recovery is the structural and functional integrity of the corticospinal tract (CST) [3].

EEG can be used to measure the activity in the motor areas of the brain. Hence, EEG can provide functional information about the CST, as the motor areas are connected to the rest of the body via the CST. Moreover, a number of correlations have been found between motor recovery and EEG measurements such as

the power ratio of low and high frequency signals at rest [74], and the amplitude of cortical response when performing a task [5].

Diffusion MRI can reconstruct the WM bundles in the brain and thus provide structural information about the CST. In particular, the invariant metrics derived from the DT have been linked to motor recovery. For example, the degree of FA asymmetry [3] and an increase in axial diffusivity (AD) have been found to correlate with motor recovery [4]. Alternatively, tractography has been used to asses the connectivity and continuity of the CST and other bundles related to motor function [4].

2.11. Relevance to this work

The methods and concepts described in this chapter contain some key points that can be related to the aim of this thesis. First of all, the presence of complex fiber orientations introduces a need for diffusion models that can describe Non-Gaussian diffusion. In this thesis, we will address this through the use of multi-compartment models which provide compartment specific measures such as the FA, as can be found in [24].

Naively applying the compartment models to the data results in overfitting due to voxels with a single fiber population. As such, some type of model selection is needed to either give an a-priori estimate of the fiber orientations or choose the model that best represents the data. Our aim is to use a model selection method that is objective and requires little a-priori knowledge as an input (as opposed to [35, 52]). Therefore, we will use parsimonious model selection which selects the models only based on the fit of the models with the data.

The fiber orientations that are obtained after this process of model fitting and selection can be used for tractography. However, the uncertainty in the data should be taken into account to mitigate the erroneous reconstruction of WM bundles, hence a probabilistic tractography algorithm should be used. We aim to capture this uncertainty by using an uncertainty measure derived from the model fitting procedure, the Cramér-Rao lower bound, which represents the lowest possible variance of the model parameters given the data [75].

Lastly, the whole framework of tractography and model selection that will be developed in this thesis should be applicable to data from stroke patients. Hence, our algorithm should be able to reconstruct measures such as FA and connectivity of motor bundles to allow for quantitative assessment of stroke related biomarkers that have been found in literature [3, 4]. Furthermore, the algorithm should take dipole locations that are found using EEG as an input. Ultimately, this could be used to relate the stroke predictors found using EEG to the biomarkers found using dMRI.

3

Methods

3.1. Models

The measured signal in a voxel S_j was basically modeled to originate from up to two fiber compartments and an isotropic compartment:

$$S_j = S_0 \left(\sum_{i=1,2} f_i \exp(-b_j \boldsymbol{g}_j^T \boldsymbol{D}_i \boldsymbol{g}_j) + f_{iso} \exp(-b_j D_{iso}) \right), \tag{3.1}$$

where S_0 denotes the signal without diffusion weighing, f_i and f_{iso} are the volume fractions of the different compartments, b_j stands for the strength of the diffusion gradient of the corresponding gradient direction $\boldsymbol{g}_j$, $\boldsymbol{D}_i$ is the 3 x 3 diffusion tensor of each fiber compartment, and lastly D_{iso} denotes the isotropic diffusion coefficient [24].

3.1.1. Parameters and constraints

Practically, we fitted nine different diffusion models of increasing complexity to the data, see Table 3.1. These models were based on the signal model of Equation (3.1). In the most conventional one, a single tensor model, we parametrized the diffusion tensor $\boldsymbol{D}_i$ with its eigenvalues λ_1, λ_2 and λ_3, and three angles θ, ϕ and ψ determining the tensor's orientation. Here, θ and ϕ represented the orientation of the principle eigenvector in spherical coordinates, see Figure 3.1a. The third angle ψ determined the rotation of the second and third eigenvectors around the first eigenvector, see Figure 3.1b. The described single tensor model can be expanded by adding an isotropic compartment.

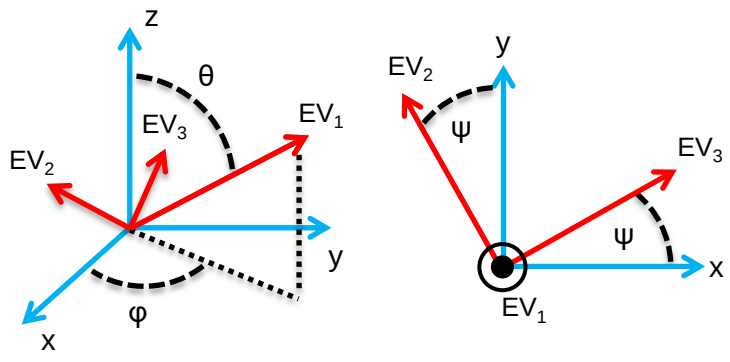

(a) (b)

Figure 3.1: Schematic representation of (a) the parametrization of the first eigenvector using spherical coordinates and (b) the rotation of the second and third eigenvector around the first eigenvector.

Table 3.1: Summary of the diffusion tensor models, their parameters and constraints

Model	Parameters	# Comp	Iso	Extra constraints
1	$\theta_1, \phi_1, \psi_1, \lambda_1, \lambda_2, \lambda_3, S_0$	1	No	
2	$\theta_1, \phi_1, \lambda_\parallel, \lambda_\perp, S_0$	1	No	$\lambda_2 = \lambda_3 = \lambda_\perp$
3	$\theta_1, \phi_1, \psi_1, \lambda_1, \lambda_2, \lambda_3, f, S_0$	2	Yes	
4	$\theta_1, \phi_1, \psi_1, \lambda_1, \lambda_2, \lambda_3, f, S_0$	2	Yes	$\lambda_1 + \lambda_2 + \lambda_3 = \text{MDC}$
5	$\theta_1, \phi_1, \lambda_\parallel, \lambda_\perp, f_{iso}, S_0$	2	Yes	$\lambda_2 = \lambda_3 = \lambda_\perp$
6	$\theta_1, \phi_1, \theta_2, \phi_2, \lambda_\parallel, \lambda_\perp, f_1, S_0$	2	No	$\lambda_{\perp_1} = \lambda_{\perp_2} = \lambda_\perp$
7	$\theta_1, \phi_1, \theta_2, \phi_2, \lambda_\parallel, \lambda_\perp, S_0$	2	No	$f_1 = f_2 = 0.5$
8	$\theta_1, \phi_1, \theta_2, \phi_2, \lambda_\parallel, \lambda_\perp, f_{iso}, f_1, S_0$	3	Yes	$\lambda_{\perp_1} = \lambda_{\perp_2} = \lambda_\perp$
9	$\theta_1, \phi_1, \theta_2, \phi_2, \lambda_\parallel, \lambda_{\perp_1}, \lambda_{\perp_2}, f_{iso}, f_1, S_0$	3	Yes	$\lambda_{2i} = \lambda_{3i} = \lambda_{\perp i}$

Further constrained versions of the signal model of Equation (3.1) were used to characterize the signal in a crossing of two fibers. While doing so, we assumed that the axial diffusivities $\lambda_\parallel$ of the two anisotropic tensors are equal. Furthermore, the second and third eigenvector of each tensor were also taken to be the same and henceforth referred to as the radial diffusivity $\lambda_\perp$. We applied these constraints in the same way as in [24], to avoid degeneracy of the parameter estimation with our data.

Other constraints that were used in the models: the isotropic diffusion coefficient was set to that of free water 3×10^{-3} mm^2/s and the sum of the volume fractions was set to one. The different diffusion models were fitted by maximum likelihood estimation assuming Rician distributed noise as in [76]

3.2. Model Selection

Clearly, unconstrained fitting the two tensor model in a region with just a single fiber population still results in overfitting. Therefore, we performed model selection with the aim to find the tensor model that best represents the underlying fiber population in each voxel.

3.2.1. ICOMP-TKLD

We adopted the ICOMP-TKLD criterion for the model selection [77]. This criterion is an adapted version of the information complexity (ICOMP) criterion [78]. The ICOMP-TKLD criterion performed model selection through balancing the goodness of the model fit and the model complexity. The goodness of fit was quantified by the log-likelihood of the model fit error. In general, the goodness of fit is improving with increasing complexity.

The model complexity was captured in the total Kullback-Leibler divergence (TKLD) [79]. This TKLD quantifies the interdepedance between the model parameters, which is a direct measure of the model complexity. In other words, the more interdependent the parameters are, the higher the model complexity. Accordingly, a model in which the parameters are orthogonal and thus independent will have a complexity of zero [80].

Formally, the ICOMP-TKLD criterion was defined as:

$$\text{ICOMP}_{\text{TKLD}}(\hat{\boldsymbol{\theta}}_{\boldsymbol{i}}) = -2\log\left(L(\hat{\boldsymbol{\theta}}_{\boldsymbol{i}}|\widetilde{\boldsymbol{S}})\right) + 2C_{tot}\left(\boldsymbol{I}^{-\mathbf{1}}(\hat{\boldsymbol{\theta}}_{\boldsymbol{i}})\right). \tag{3.2}$$

Here, the first term quantified the goodness of fit where L is the likelihood of the fit of the parameter vector $\hat{\boldsymbol{\theta}}_{\boldsymbol{i}}$ given the measured signal $\widetilde{\boldsymbol{S}}$. The second term represents the model complexity, where C_{tot} denotes the TKLD which requires the inverse of the Fisher information matrix I^{-1} as an input.

3.3. Uncertainty in the fiber orientation

The previously described model selection essentially outputted the most appropriate model as estimates for the fiber orientation(s) in each voxel. These served as an input for our probabilistic tractography algorithm. The probabilistic tractography algorithm also needed a measure of the uncertainty in the estimated fiber orientations. In this work, we used the Cramér-Rao lower bound (CRLB) in the solution of each model parameter to provide an estimate of the variance in the estimated fiber orientations. This CRLB was obtained by inverting the Fisher information matrix. The diagonal of the resulting matrix contained lower bounds for the variance that could be obtained by an unbiased estimator on the given data [75].

In our diffusion tensor models the angles θ and ϕ determine the fiber orientation. The uncertainty in these parameters was assumed to be normally distributed with a mean equal to the estimated parameter value, a variance equal to the CRLB of the parameter and a covariance obtained from the off-diagonal elements of the CRLB matrix. This yielded a probability density function (PDF) of the fiber orientations at each voxel, that were sampled during tractography.

3.4. Tractography algorithm

Our tractography algorithm is a standard line propagation algorithm with a fixed step size [56]. The probabilistic aspect of the tractography was reflected in the placement of seed points and the sampling of the fiber orientation PDFs from the fiber compartment(s) at each step. The starting points for the streamlines were placed at a random position inside the seed voxels, as this allowed us to sample the variation in streamlines based on their starting position. The streamlines were propagated by comparing the direction of the last step in the streamline with a sample from the fiber orientation PDF of each compartment in the voxel. A step was taken in the direction of the sample that made the smallest angle with the previous step. Propagation of the fiber was stopped when the angle between successive steps was larger than a curvature threshold, the streamline exited the brain mask or the streamline looped back on itself. Additionally, exclusion masks and waypoints can be used with the algorithm to filter out specific (un)wanted streamlines. In general, we generated 5000 streamlines per seed voxel to obtain sufficient sampling of the fiber orientation PDFs.

3.5. Model selection validation

The model selection methods had to be validated to assure proper performance in regions with complex fiber orientations, i.e. select the model with the correct amount of fiber compartments. Therefore, we used a dataset known as the fibercup phantom, which mimics the fiber configuration in a coronal slice of the brain (see Figure 3.2). Specifically, we used a reconstructed version of the fibercup phantom which has more realistic diffusivity values [81]. This dataset consists of a 64 x 64 x 3 volume of isotropic 3 mm^3 voxels at 3 different diffusion weightings, 650, 1500 and 2000 s/mm^2, with each 65 gradient directions. Importantly, the underlying ground truth of the fibercup phantom is known, thus it allows for voxel-wise validation of the selected models. The performance of the model selection was evaluated with respect to three parameters that could influence the model fit: the b-value, the model parametrization, and the noise level. Additionally, we performed a qualitative comparison on human data to obtain an insight into the in-vivo behavior of our model selection.

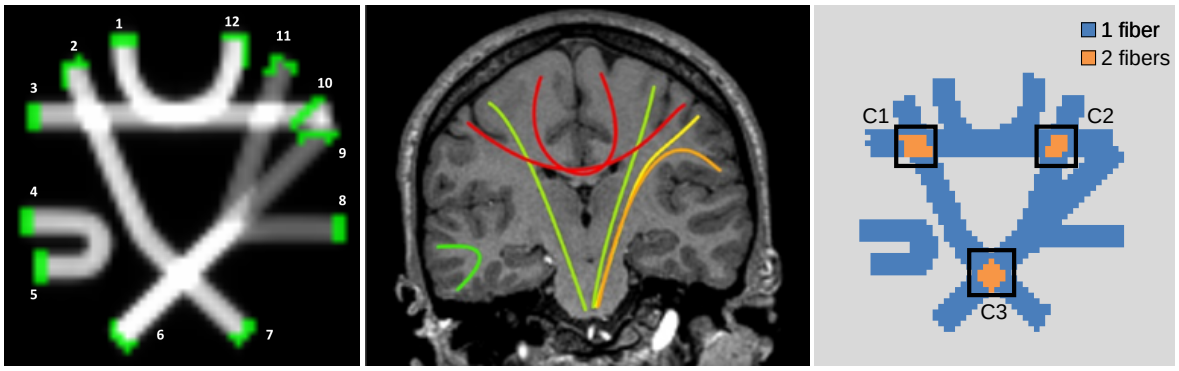

(a) (b) (c)

Figure 3.2: (a) The fibercup phantom with numbered ROIs; (b) A coronal slice of the brain with the WM bundles that are mimicked by the fibercup, adapted from [82]; (c) The ground truth of the number of fiber compartments at each position with numbered fiber crossings (C1-C3).

3.5.1. b-values

As mentioned before, the b-value determines the sensitivity of the dMRI acquisition to diffusion. For the 3D diffusion profile this means that the b-value influences the ability to distinguish crossing fibers. Particularly, a higher b-value will lead to a larger difference between the signal attenuation along and across the fiber orientations as is visualized in Figure 3.3 [83].

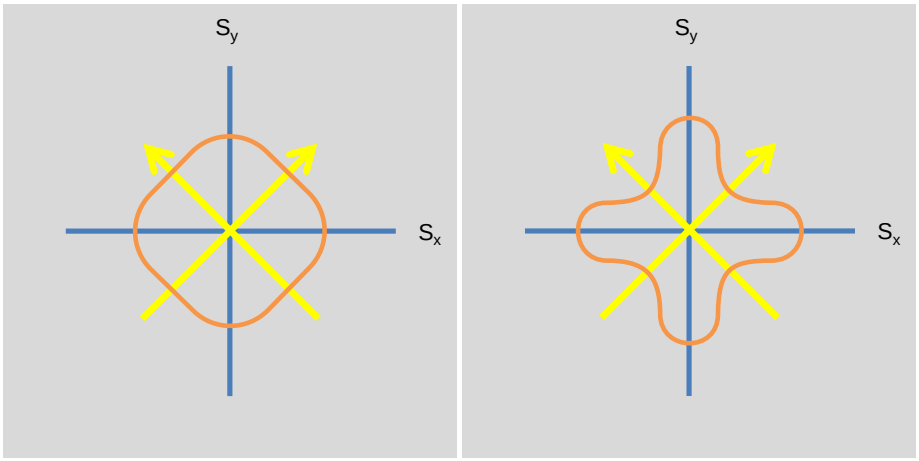

(a) (b)

Figure 3.3: Schematic drawings of the 2D diffusion signal profile in a crossing for (a) a low b-value and, (b) a higher b-value. The yellow arrows indicate the fiber directions whilst the orange line represents the diffusion signal.

The changing shape of the diffusion profile with b-value affects the fit of the model and thus also affects our model selection method. In the case of our models, at least 2 b-values are needed to independently estimate the diffusion profiles [24]. Therefore, we compared the effect of using different combinations of b-values on the ability of our model selection method to detect crossing fibers. In practice, we used 4 different combinations of at least 2 b-values. Ultimately, this comparison will help us identify the optimal b-values for the in-vivo application of the model selection.

3.5.2. Model parametrization

The orientation of the eigenvectors can be parametrized in a number of ways. In this work, the models were chosen to have a similar parametrization of these eigenvectors as this allows for a fairer comparison between the models. The original parametrization of models 1, 3 and 4 (Table 3.1) used to be different. Specifically, the orientation of the eigenvectors was defined using the concepts of yaw, roll and pitch (α_1, α_2 and α_3), as can be seen in Figure 3.4. Moreover, all these 3 angles were used to describe the orientation of the principal eigenvector (EV_1). In comparison, our parametrization included only 2 angles to describe this eigenvector.

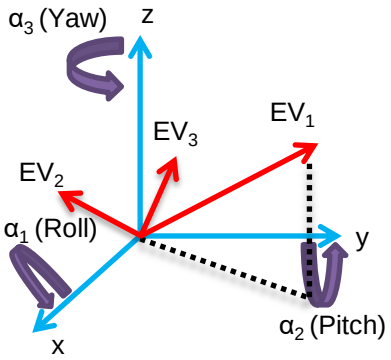

Figure 3.4: Parametrization of the eigenvectors by yaw, roll and pitch.

Supposedly, the complexity criterion used in our model selection, the TKLD, is independent of the coordinate system [80], hence a reparametrization of our models should result in a similar output of the model selection. Importantly, this allowed us to check whether our parametrization of models 1, 3 and 4 was equivalent to the original parametrization. Therefore, we replaced 3 of the input models of the model selection (model 1, 3 and 4) with the original parametrization and compared the output before and after replacement. We used the fibercup data with the optimal b-values to perform this comparison.

3.5.3. Noise

Noise also influences the model fit, as it decreases the contrast between the peaks and valleys in the signal profile. The fibercup data is relatively noise free while in reality dMRI-acquisitions are quite noisy. Hence, noise has to be added to the fibercup data to be able to asses the behavior of our model selection method with noise. We used 2 levels of noise which are shown in Table 3.2. Furthermore, the SNR in this work will be reported per b-value and is determined by:

$$\text{SNR} = \frac{\text{median}(S_{\text{brain}})}{\sigma_{\text{noise}}}. \tag{3.3}$$

Table 3.2: Signal-to-noise ratios for the different noise scenarios

	b = 0	b = 1500	b = 2000
Noise scenario 1 (N1)	39	11	7
Noise scenario 2 (N2)	26	7	5

3.5.4. In-vivo

The in-vivo validation was performed on data from 7 healthy controls with multiple b-values: 1000 and 2000 s/mm^2. The scans were acquired on a 3T MRI scanner (Discovery MR750, GE Medical Systems). 40 gradient directions were used for the diffusion weighted acquisitions combined with five non-diffusion weighted acquisitions per b-value. Furthermore, the SNR values for the b = 0, 1000, and 2000 s/mm^2 acquisitions were estimated to be 41, 20 and 12 respectively.

Particularly, we visually compared the outputs of the model selection in the crossing of the corticospinal tract and the corpus callosum, which is a structure also modeled by the fibercup phantom (see Figure 3.2(b,c)). Importantly, all the outputs were registered to MNI-space to allow for a sound comparison.

3.6. Sensitivity analysis

In the literature part of this thesis we already mentioned that the behavior tractography algorithms depends on parameters such as the propagation method and stopping criteria. Therefore, we studied the effects of these parameters on the output of our tractography algorithm by performing a sensitivity analysis. Specifically, we studied the effect of the step size and the curvature threshold.

3.6.1. Tractometer measures

The fibercup phantom (b= 1500, 2000 s/mm^2) was used to perform the sensitivity analysis using measures from the tractometer, which is an online evaluation tool for tractography algorithms [82]. These measures assessed the performance of the algorithm by quantifying global measures, such as the percentage of the valid bundle covered by streamlines (Average bundle coverage or ABC), the percentage of invalid bundles covered by streamlines (No bundle coverage or NBC) and, the angular error of the generated streamlines. ROI specific measures that were used were the number of streamlines that either correctly connect ROIs (Valid connections or VC), do not reach another ROI (No connection or NC) and incorrectly connect ROIs (Invalid connections or IC).

We investigated the behavior of these tractometer measures for a range of 5 different step sizes (0.25, 0.5, 1, 2 and 3 mm) and 3 curvature thresholds (45°, 60° and 80°). Furthermore, a baseline (BL) tractography was performed, i.e. without additional noise, as well as tractography for noise scenario 1 (see Table 3.2) to investigate the change of sensitivity under the influence of noise. Importantly, we used noise scenario 1 because its SNR is comparable to the SNR of our human data.

3.6.2. In-vivo

In practice, the tractography algorithm should not only propagate through the white matter bundles, as is the case in the fibercup phantom, but also through the gray matter. Therefore, we performed an additional sensitivity analysis by investigating the performance of our tractography algorithm in the corticospinal tract (CST). Importantly, we used the CST because of its relevance to stroke and its trajectory in the brain, which ends in the gray matter.

The tractography was limited to one hemisphere of the brain to allow for a clear visualization of the effects of step size and curvature threshold. Seed regions were placed at the bottom of the CST. Furthermore, we used 3 different step sizes (0.09, 0.5 and 0.9375 mm) and 3 curvature thresholds (45°, 60° and 80°). In total, 43 seed points were used with 5000 streamlines generated per seed point.

3.7. Benchmarking

The performance of our tractography algorithm was assessed by comparing it with the open source dMRI toolkit Camino [10] . We used this toolkit due to its similarities to our proposed framework: Camino also allows for model selection and probabilistic multi-fiber tractography using multi-tensor models. However, the model selection in Camino differs from our method as it uses the type of diffusion present in a voxel, e.g. Non-Gaussian or Gaussian diffusion, to specify whether a single or dual tensor model can be used [52]. Furthermore, we used the Camino's built-in multi-tensor models with eigenvalues that were constrained to be positive. The probabilistic tractography in Camino was performed using its PICo tractography algorithm with 5000 streamlines per seed point and a curvature threshold of 80 degrees. The optimal step size for tractography was determined for both methods and was found to be 0.5 mm for our method and 1.5 mm for Camino.

We performed a quantitative and qualitative comparison between the two tractography frameworks. In the quantitative comparison we used the reconstructed version of the fibercup phantom [81] with multiple b-values (1500/2000 $mm^2\ s^{-1}$). Furthermore, we evaluated the performance of the two tractography algorithms by assessing the output of the aforementioned tractometer measures. We again performed a baseline (BL) tractography, as well as tractography at range of SNR values to investigate the sensitivity of the tractography algorithms to noise (Table 3.2).

The qualitative comparison was performed on data from 5 of the 7 healthy controls with multiple b-values (1000, 2000 s/mm^2). Seed regions were placed in the corticospinal tract (CST) and the corpus callosum (CC). We examined the lateral projections of the CC into the pre-central gyrus to asses the performance of the methods on in-vivo fiber crossings.

3.8. Application to EEG sources

We investigated the feasibility of combining our tractography framework with source locations obtained from EEG recordings. For this, we used EEG data obtained from the department of Biomechatronics & Human-Machine Control at the faculty of Mechanical, Maritime and Materials Engineering (3ME) at the TU Delft. In these EEG recordings, the brain activity in a subject was measured while a robotic manipulator applied disturbances to the wrist. At the same time, the subjects performed tasks which consisted of relaxing the wrist and ignoring the disturbances, or maintaining a certain amount of wrist flexion during the disturbances [5]. The sources that were persistent during these task were extracted from the EEG recording by performing an independent component analysis (ICA). Furthermore, subject specific head models were used to reconstruct the locations of the sources in the brain. The source locations were registered to MNI space to allow for comparison between the subjects. The received EEG data consisted of 5 patients whom have had an ischemic stroke, and 6 healthy controls. Furthermore, the amount of sources per subject ranged from 8 to 12.

The source locations, which are also known as dipoles, can be used to investigate anatomic connections between the sources. The anatomic connections between all the different dipoles in the brain form a brain network. In general, such a brain network can be represented by a collection of nodes in the form of brain regions, which are connected via links formed by the anatomical connections between these regions. Additionally, the brain networks can be subdivided into groups of densely interconnected brain regions. This type of subdivision of the brain network is known as the modular structure of the network. Furthermore, the groups of densely interconnected brain regions are known as modules and grouped by maximizing the within group links and minimizing the between group links [84].

A stroke might induce changes in the modular structure, as it affects the connections between the brain regions. Therefore, we used our tractography framework to investigate the anatomical connections and the modular structures they form by generating streamlines originating from the dipoles. The anatomical connections were quantified by counting the streamlines traveling from one dipole to the other and vice-versa. Furthermore, the dipoles were transformed from MNI-space into patient space to serve as seed points for the tractography. Importantly, we used spherical seed regions with a radius of 5 mm, centered at the dipole location, to capture the uncertainty in the dipole location, which resulted in 227 seed voxels per dipole. We generated 5000 streamlines per seed voxel with a step size of 0.5 mm. Furthermore, a curvature threshold of

80° and a maximum streamline length of 1 m were used as stopping criteria. Streamlines with a length shorter than 6 mm were excluded, as these were assumed to be anatomically implausible.

Additionally, we mapped the dipoles to a cortical atlas to allow for an inter-subject comparison of the connections between different cortical regions. For this, we used an MNI-atlas of Brodmann areas (A standard template in MRICron [85]), which subdivides the cortex based on the tissue structure at a cellular level (Figure 3.5). Table 3.3 shows a selection of the Brodmann areas, which relate to brain regions relevant in our patient group.

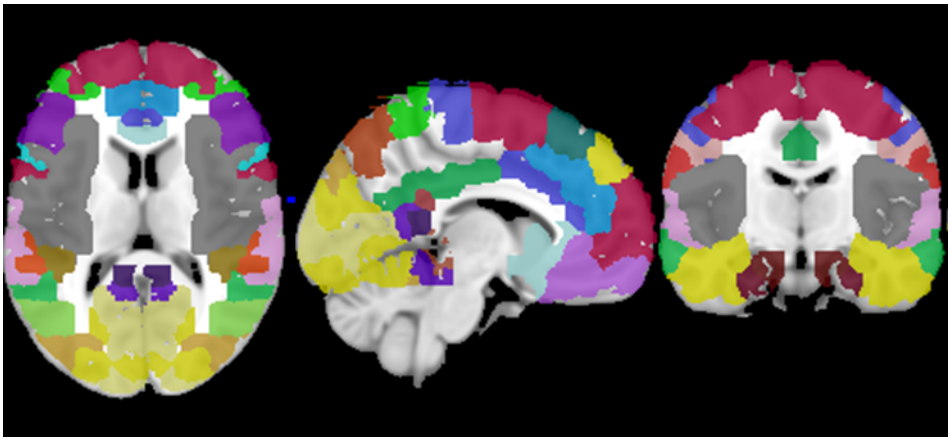

Figure 3.5: Orthogonal slices of the Brodmann atlas used for the dipole mapping. The atlas is overlayed on the MNI-152 T1-weighted brain template. Each different color represents a different Brodmann area.

Table 3.3: A selection of Brodmann areas with relevance for our patient group and their corresponding anatomical regions.

Brodmann Area	**Anatomical region**
1, 2 and 3	Sensory cortices
4	Primary motor cortex
5 and 7	Sensorimotor areas and association cortices
6	Premotor cortex

Connectivity matrices for each subject group (Patients/controls) were obtained by summing the streamline counts of the connections between the different Brodmann areas. From these connectivity matrices, we determined the modular structure in each subject group. Specifically, we used an algorithm from the brain connectivity toolbox for MATLAB [84] that subdivides a brain network with directed links into modules by using the modularity statistic [84]. For both subject-groups, the algorithm was set to use the classic modularity as criterion.

4

Results

4.1. Model selection validation

4.1.1. B-values

Table 4.1 summarizes the performance of our model selection methods for the different combinations of b-values. In this table, we see that only one combination (b= 1500, 2000 s/mm^2) of b-values led to a selection of multiple fiber compartments in all crossing regions. In this case, 85.8 % (109 out of 127) of the multi-fiber voxels was identified correctly. Furthermore, the fiber orientations found by the selected diffusion models seems to correspond to the ground truth, as can be seen in Figure 4.1(a).

Table 4.1: Results for the amount of multi-fiber voxels and fiber angle between the fibers for each crossing (C1-C3) for different combinations of b-values.

	C1		C2		C3	
	voxels (#)	Fiber angle (°)	voxels (#)	Fiber angle (°)	voxels (#)	Fiber angle (°)
Ground truth	43	67.96 (± 0.080)	36	71.38 (± 0.064)	48	87.21 (± 0.57)
b = 650, 1500	3	89.31 (± 0.55)	0	x	28	87.29 (± 0.55)
b = 650, 2000	4	73.47 (± 11.0)	0	x	27	87.27 (± 0.54)
b = 650, 1500, 2000	2	68.10 (± 0.0098)	0	x	26	87.29 (± 0.59)
b = 1500, 2000	35	69.30 (± 0.55)	32	73.55 (± 1.04)	42	87.45 (± 0.58)

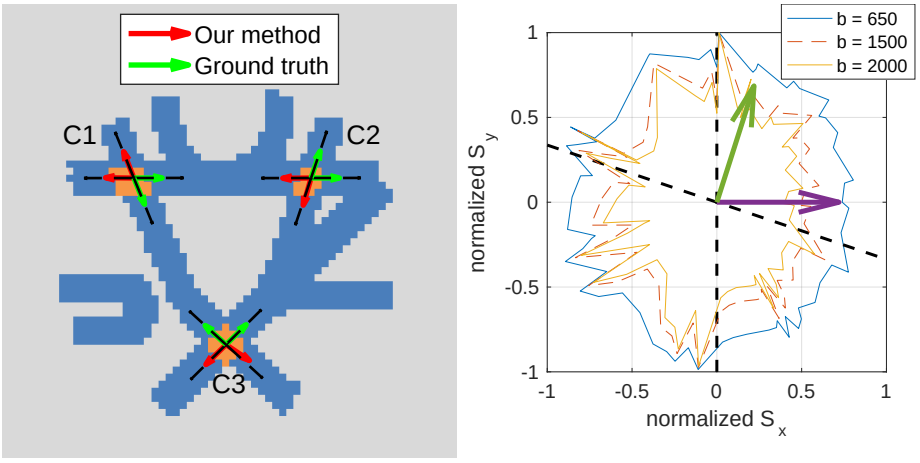

(a) (b)

Figure 4.1: (a) Comparison between the mean fiber orientations reconstructed in the crossings by our method (b=1500, 2000 s/mm^2) and the fiber orientations from the ground truth. The black dashed line indicates the fiber orientation in the ground truth; (b) Projections to the xy-plane of the diffusion signal in C2 for the different b-values. The black dashed lines indicate the orientations along which we can expect a signal maximum and the arrows depict the underlying fiber orientations.

Our model selection did not select any multi-compartment models in crossing C2 for the other b-value combinations. We investigated the radial dependence of the signal to asses whether the crossing fibers could be distinguished, see Figure 4.1(b). Here, the signal profile for the b = 650 s/mm^2 showed only a small difference in the signal attenuation along and across the fiber orientations when compared to the other b-values. Consequently, crossing fibers were harder to distinguish at this b-value.

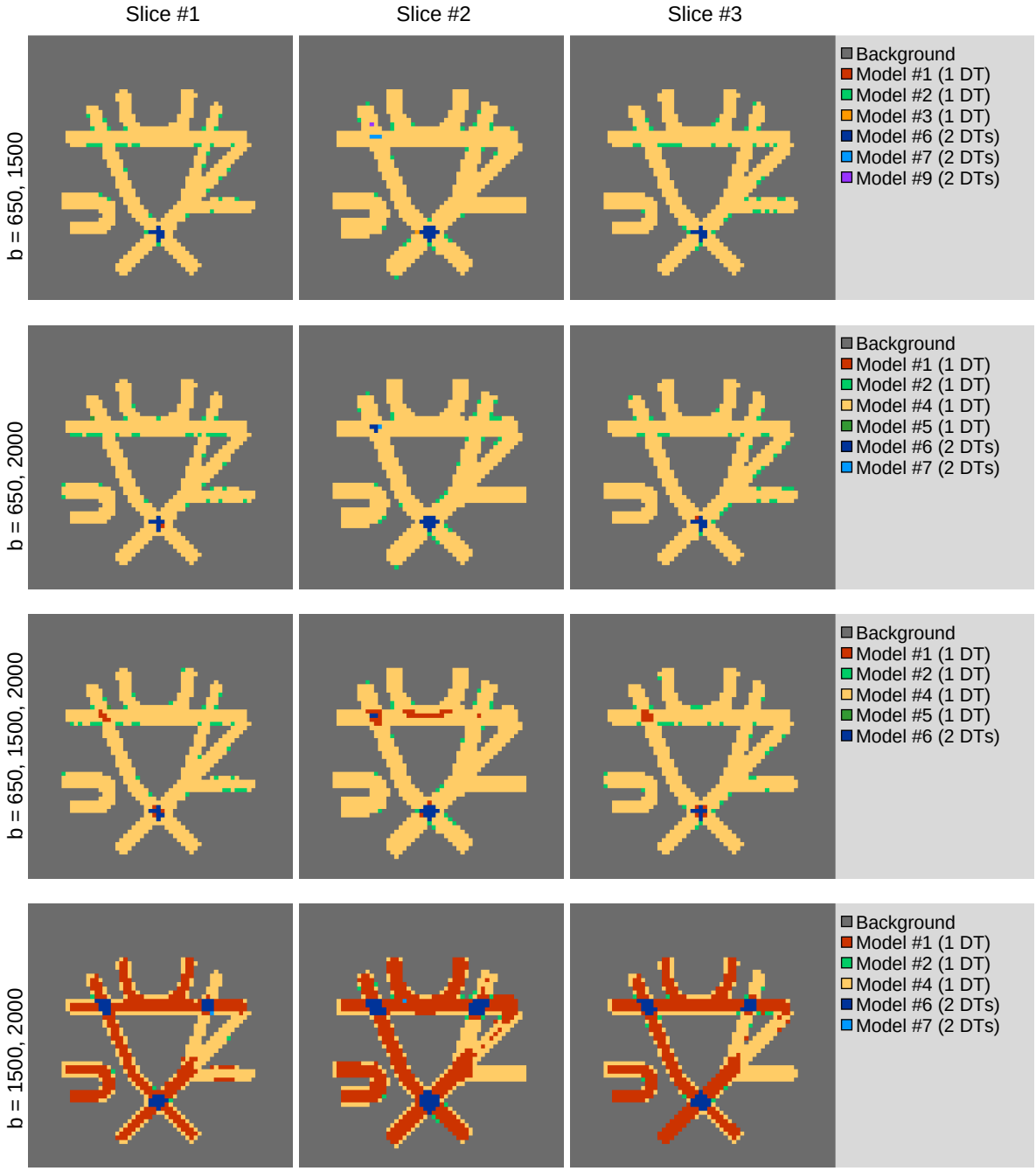

Figure 4.2: The diffusion model selected per voxel for different combinations of b-values.

Figure 4.2 shows the models selected by our model selection in each voxel for the different b-value combinations. In principle, we want the model selection to select either model 6, 7, 8 or 9 in the regions with multiple fibers from Figure 3.2(c), as these are all models with multiple anisotropic compartments. Overall, we can see that only crossing C3 was resolved for all different b-value combinations. Notably, this was the crossing with fibers that cross at an angle of nearly 90°.

The models selected within the white matter bundles were markedly different for the b-value combination of b = 1500 and 2000 s/mm^2. Specifically, model 1, a single tensor model without an isotropic compartment, was selected in the white matter bundels, whereas model 4, a single tensor model with an isotropic compartment, was only selected at the edges of the bundles. Conversely, model 4 was selected in the white matter bundles for the other b-value combinations. For b = 1500 and 2000 s/mm^2, model 1 had a better goodness of fit in the white matter bundles, whereas model 4 had a better goodness of fit in the same region for all the other b-value combinations.

4.1.2. Parametrization

The effect of using a different parametrization is shown in Figure 4.3. The different parametrization led to the selection of model 2, a single tensor with cigar-shape without an isotropic compartment, instead of model 1 when compared our parametrization. Nevertheless, the percentage of correctly identified multi-fiber voxels was the same, at 85.8%, as in the original parametrization. Additionally, the estimated fiber orientations still matched the ground truth, as can be seen in Table 4.2.

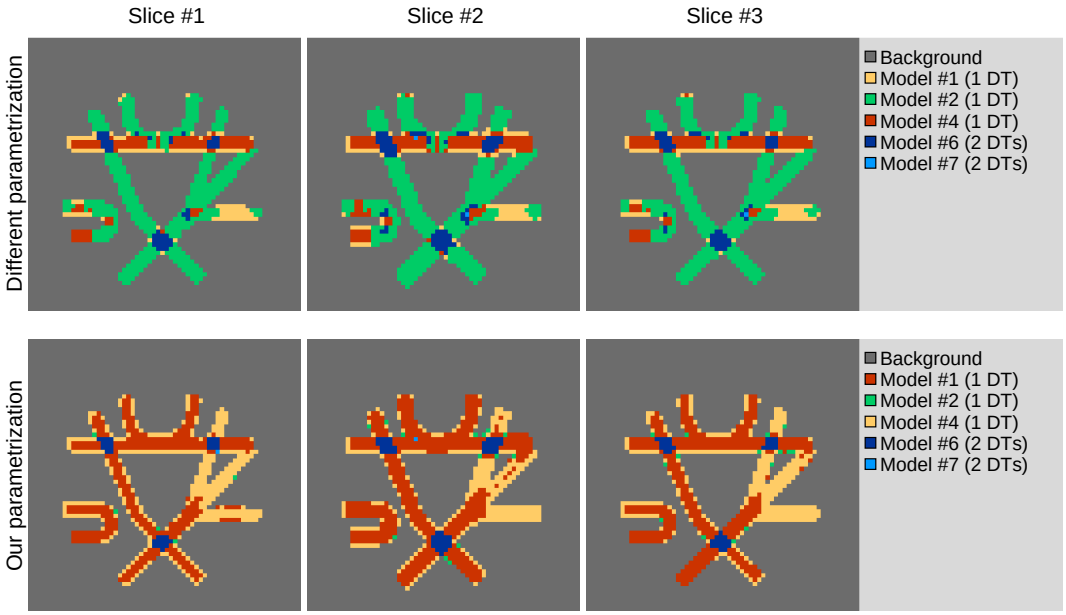

Figure 4.3: The diffusion model selected per voxel for the different model parametrizations both have b-values of 1500 and 2000 s/mm^2.

Table 4.2: Results for the amount of multi-fiber voxels and fiber angle between the fibers for each crossing (C1-C3) for a different parametrization and different noise scenarios.

	C1		C2		C3	
	voxels (#)	Fiber angle (°)	voxels (#)	Fiber angle (°)	voxels (#)	Fiber angle (°)
Ground truth	43	67.96 (± 0.080)	36	71.38 (± 0.064)	48	87.21 (± 0.57)
Parametrization	34	69.25 (± 0.48)	30	73.38 (± 0.74)	45	87.54 (± 0.68)
N1	33	69.64 (± 1.26)	21	73.33 (± 2.20)	39	87.55 (± 1.00)
N2	28	69.52 (± 2.31)	12	74.14 (± 1.75)	34	87.17 (± 1.61)

4.1.3. Noise

As can be seen in Figure 4.4 and Table 4.2, the number of multi-fiber voxels found by our model selection decreased with an increase in noise. Specifically, the performance in crossing C2 was affected the most by noise, as only 33.3% (12 out of 36) of the multi-fiber voxels was reconstructed for the worst noise scenario (N2). However, the decrease in performance was not limited to crossing C2. The amount of reconstructed multi-fiber voxels in crossings C1 and C3 decreased by 20% and 19%, respectively. Moreover, the average fiber orientations estimated still conformed to the ground truth. Simultaneously, the standard deviation of the angle between the fibers increased with noise (Table 4.2).

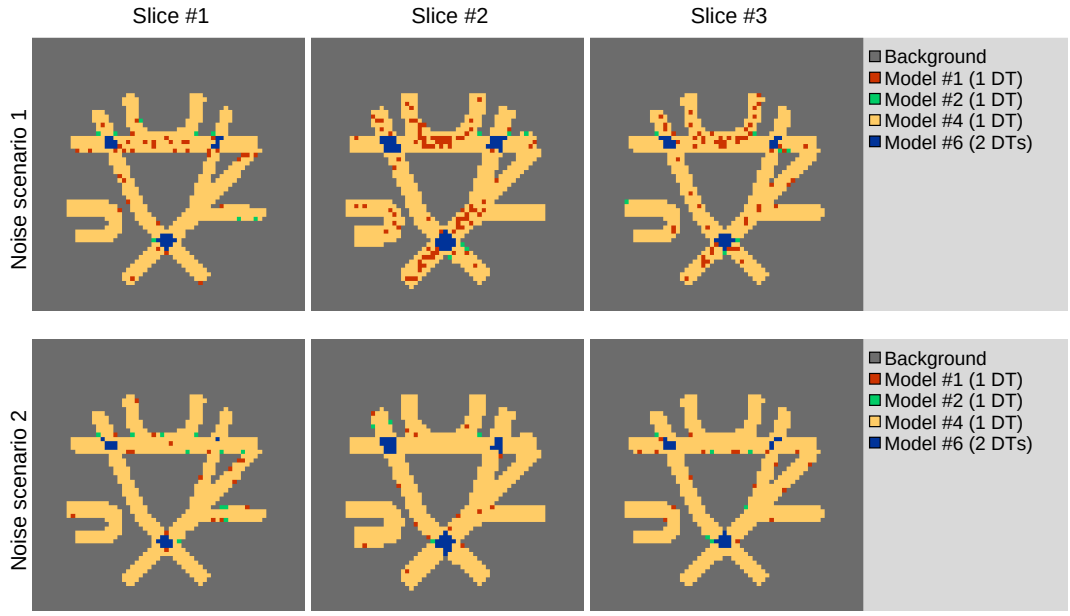

Figure 4.4: The diffusion model selected per voxel for different noise scenarios with b = 1500, 2000.

4.1.4. In-vivo

Figure 4.5 shows that the outputs of our model selection method in the crossing fiber region was similar for the 7 healthy controls. On average, our model selection method selected a model with multiple fiber compartments in 53.5% of the voxels within the red circle. Furthermore, the lowest percentage of multi-fiber models was selected in subject 19904 (Figure 4.5(c)) with 38.7%, whereas the highest percentage of multi-fiber models was selected in subject 19908 (Figure 4.5(g)) with 64.2%.

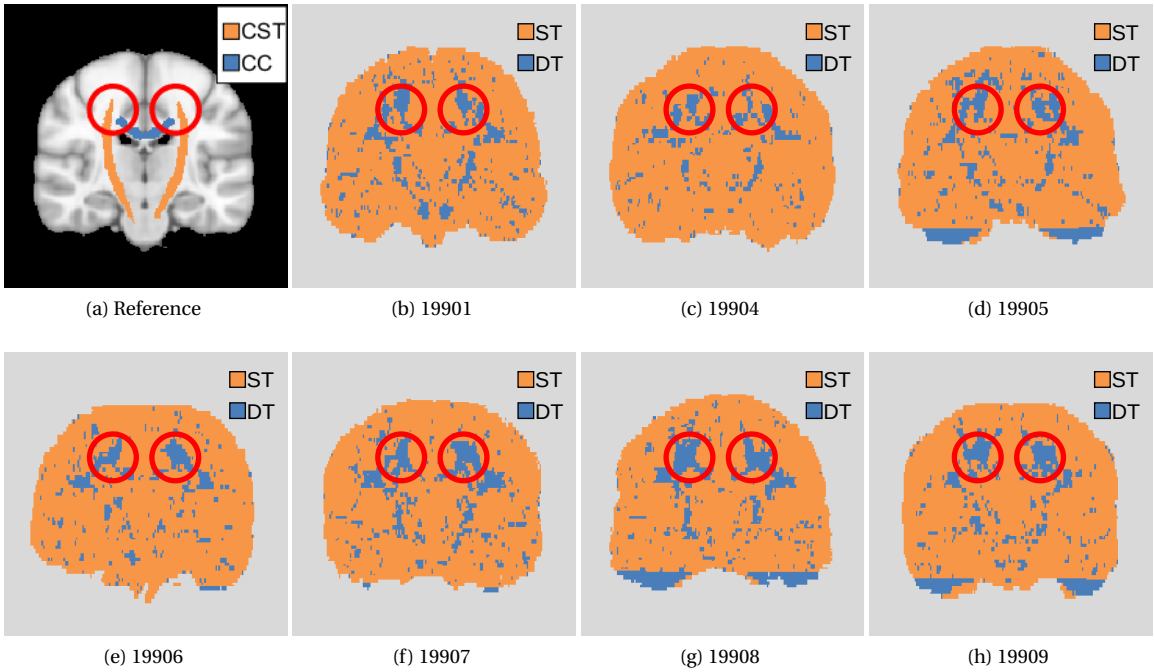

(a) Reference (b) 19901 (c) 19904 (d) 19905

(e) 19906 (f) 19907 (g) 19908 (h) 19909

Figure 4.5: (a) A coronal slice of the MNI-152 T1-weighted template image overlayed with the corticospinal tract (CST) and corpus callosum (CC). (b-h) The same slice with the output of our model selection for 7 healthy controls in terms of models with a single (ST) or multiple (DT) fiber compartments. The red circles indicate the region where fibers from the CC cross the CST.

4.2. Sensitivity analysis

4.2.1. Step size

We evaluated the effect of the step size on the collective (average) performance of the tractography on all the ROIs of the fibercup phantom by repeating the tractography algorithm 5 times for each step size. Figure 4.6 shows the effect of the step size on the different connections types (VC, NC and IC) and the angular error. In general, we want the amount of valid connections to be as high as possible while minimizing the amount of invalid connections and no connections.

First of all, the percentage of VCs decreased with increasing step size for both the baseline and noise scenario. Specifically, the VC percentage decreased from 66.4% to 1.1% for the baseline and from 58.2% to 1.7% for the noise scenario when increasing the step size from 0.25 to 3 mm. Conversely, the NC percentage increased with increasing step size for both the baseline and noise scenario with a low of 30.2 % and a high of 98.3%. Furthermore, the IC percentage showed a slight increase for the baseline tractography with increasing step size. The noise scenario had no significant increase in invalid connection percentage with increasing step size. However, on average the noise scenario tractography showed a higher IC percentage than the baseline tractography. Lastly, the angular error increased with both step size and noise level, as can be seen in Figure 4.6(d).

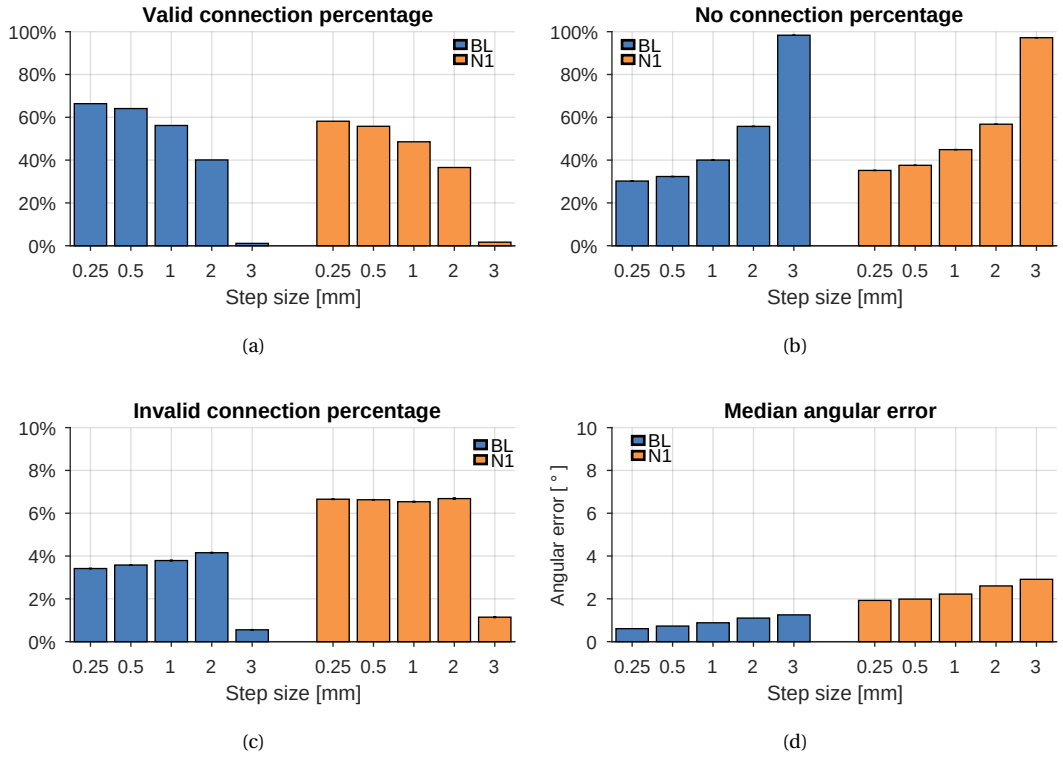

Figure 4.6: Barplots of the behavior of (a) valid connections, (b) no connections, (c) invalid connections and (d) angular error for different step sizes.

We used a Wilcoxon rank sum test to test whether the perceived performance difference between the different step sizes was significant. Specifically, we looked at the performance difference between adjacent step sizes, for example 0.25 and 0.5 mm, for the different connection types and tested whether the smaller step size performed better. Table 4.3 and Table 4.4 show that the resulting p-values for both the baseline and the noise scenario were similar. Here, we found no significant difference in performance between the two smallest step size, 0.25 and 0.5 mm. However, the smaller step size performed significantly better for all the other step size combinations. Lastly, no significant differences were found for the ICs.

Table 4.3: P-values for the comparison of the performance of our tractography algorithm with different step sizes for the baseline tractography.

	0.25 vs 0.5 mm	0.5 vs 1 mm	1 vs 2 mm	2 vs 3 mm
Valid connections	x	$7.0 \cdot 10^{-6}$	$2.0 \cdot 10^{-13}$	$1.8 \cdot 10^{-21}$
Invalid connections	x	x	x	x
No connections	x	$1.2 \cdot 10^{-5}$	$2.2 \cdot 10^{-16}$	$1.8 \cdot 10^{-21}$

Table 4.4: P-values for the comparison of the performance of our tractography algorithm with different step sizes for the noise scenario.

	0.25 vs 0.5 mm	0.5 vs 1 mm	1 vs 2 mm	2 vs 3 mm
Valid connections	x	$7.6 \cdot 10^{-3}$	$3.0 \cdot 10^{-7}$	$1.8 \cdot 10^{-21}$
Invalid connections	x	x	x	x
No connections	x	$7.5 \cdot 10^{-5}$	$1.5 \cdot 10^{-9}$	$1.8 \cdot 10^{-21}$

Figure 4.7 shows the average bundle coverage (ABC) and no bundle coverage (NBC) for the different step size. Here, The ABC seemed to only show a significant decrease for a step size of 3 mm, whereas the NBC increased slightly with step sizes up to 2 mm.

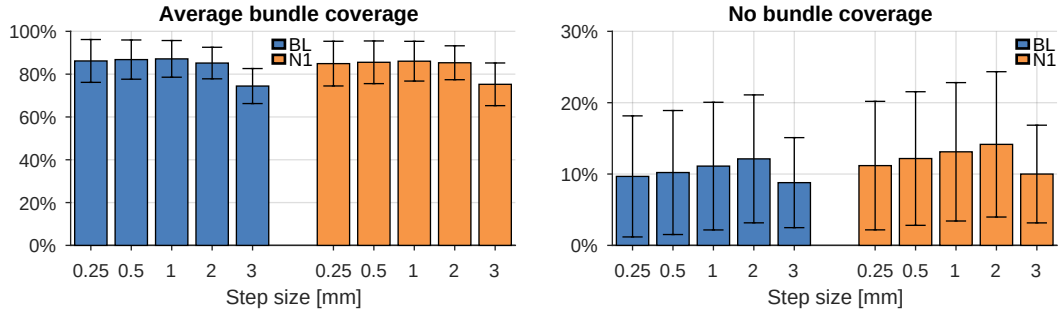

(a) (b)

Figure 4.7: Barplots of the behavior of (a) average bundle coverage and (b) no bundle coverage.

4.2.2. Curvature threshold

We investigated the effect of the curvature threshold on our tractography by repeating the sensitivity analysis for the step size with different curvature thresholds. Importantly, we repeated the tractography 5 times for each combination of step size and curvature threshold. Figure 4.8 and 4.9 show the average performance of the tractograpy on the tractometer measures over all the ROIs.

The VC percentage and median angular error (Figure 4.8(a,d)) did not seem to be affected by the change in curvature threshold, as there seemed to be little change of the VC percentage and angular error for different curvature thresholds at the same step size. Moreover, the behavior with increasing step size was found to be similar to the results from Figure 4.6(a,d). On the other hand, the IC and NC percentage did seem to be influenced by the curvature threshold, as lowering the threshold from 80 to 45 degrees maximally led to a 5% decrease in IC percentage and a similar increase in NC percentage. Notably, the effect of the curvature threshold seemed to be similar for both the baseline and noise scenario.

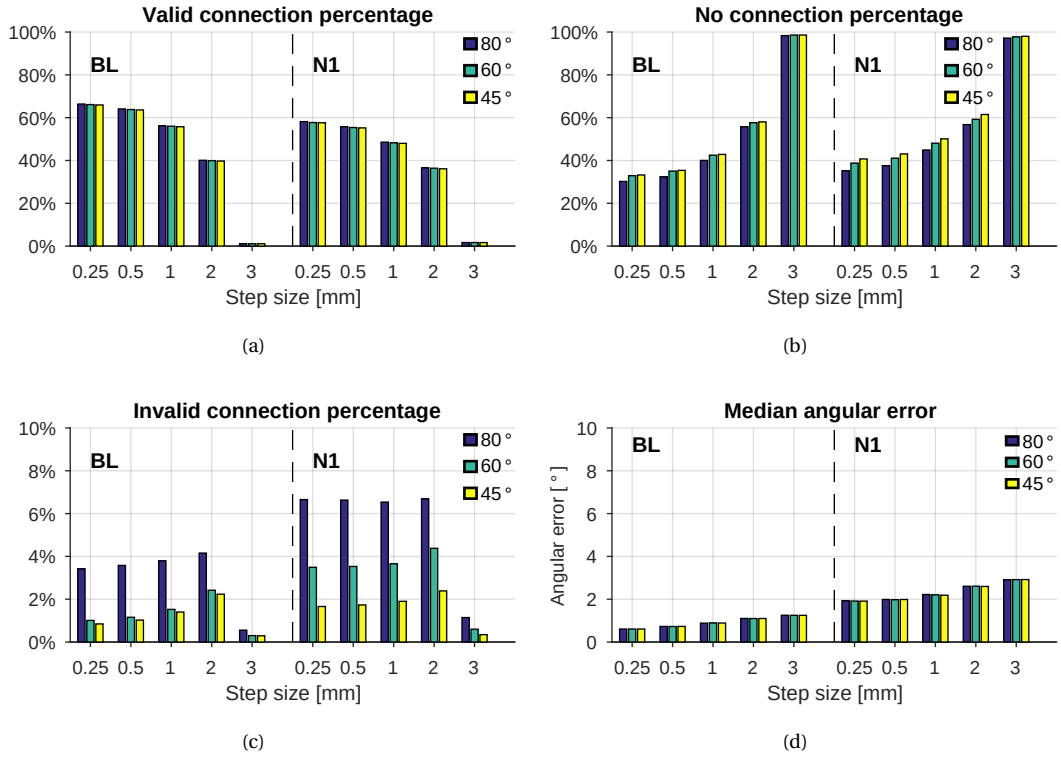

Figure 4.8: Barplots of the behavior of (a) valid connections, (b) no connections, (c) invalid connections and (d) angular error for different step sizes and curvature thresholds.

The ABC and NBC for different step sizes and curvature thresholds are shown in Figure 4.9. Here, the ABC showed similar behavior to the results from Figure 4.7(a). However, the NBC seemed to decrease with a decrease in curvature threshold.

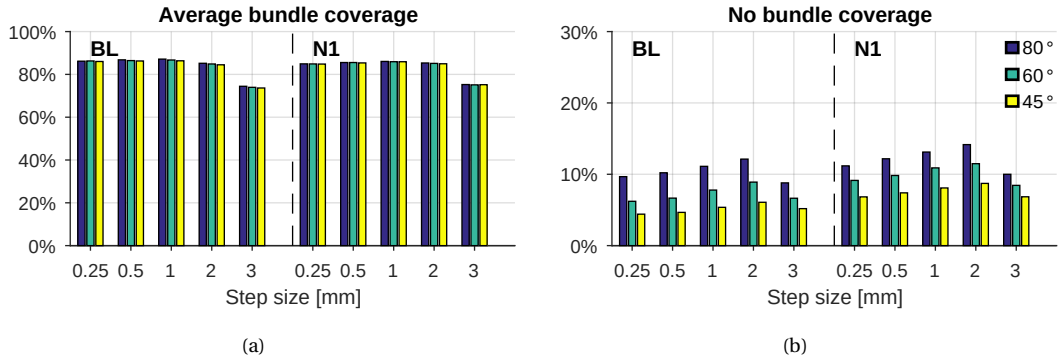

Figure 4.9: Barplots of the behavior of (a) average bundle coverage and (b) no bundle coverage for different step sizes and curvature thresholds.

4.2.3. In vivo

The influence of the step size and curvature threshold on a tractography of the corticospinal tract is shown in Figure 4.10 and 4.11. Figure 4.10 shows that an increase in both step size and curvature threshold resulted in more radial branches of the CST, which are marked by the green and red ellipses. However, the increase in curvature threshold had a larger effect than the step size on the exploration of these branches. Similarly, Figure 4.11 shows that an increase in step size and curvature threshold related to more streamlines in the frontal part of the brain (See the area within the red ellipse). Additionally, the streamlines traveled further into the gray matter for an increase in curvature threshold.

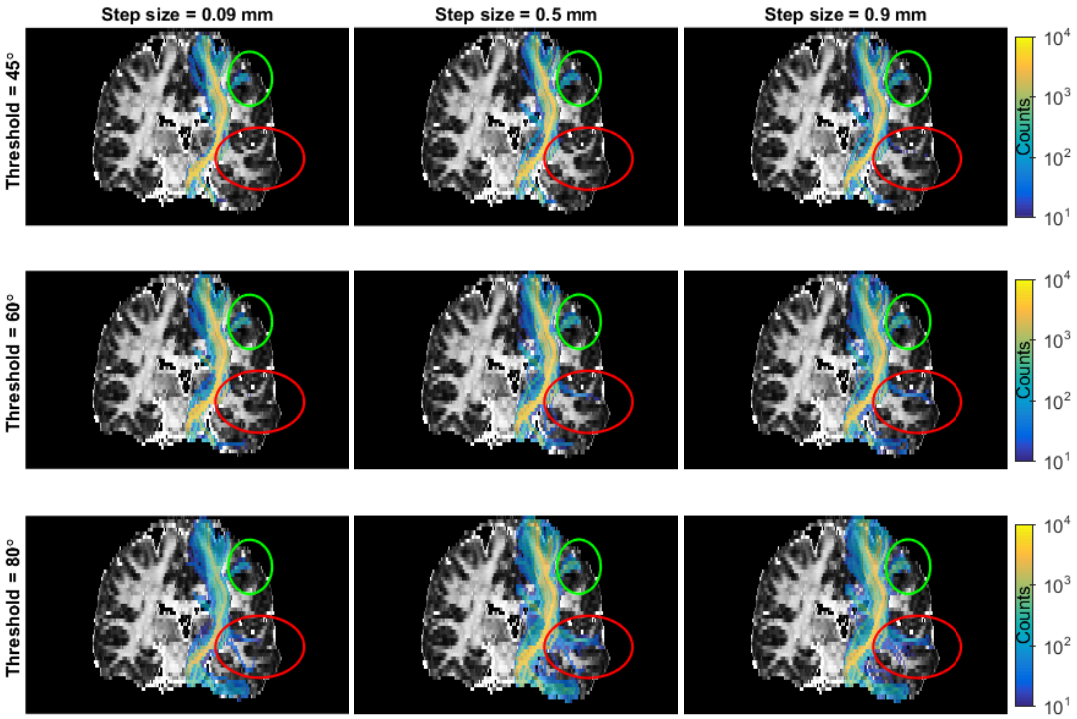

Figure 4.10: Maximum intensity projection of the streamline density in the coronal plane for different step sizes and curvature thresholds. The streamlines are overlaid on a coronal slice of a fractional anisotropy map. The green and red ellipses mark the areas most affected by the step size and curvature threshold change.

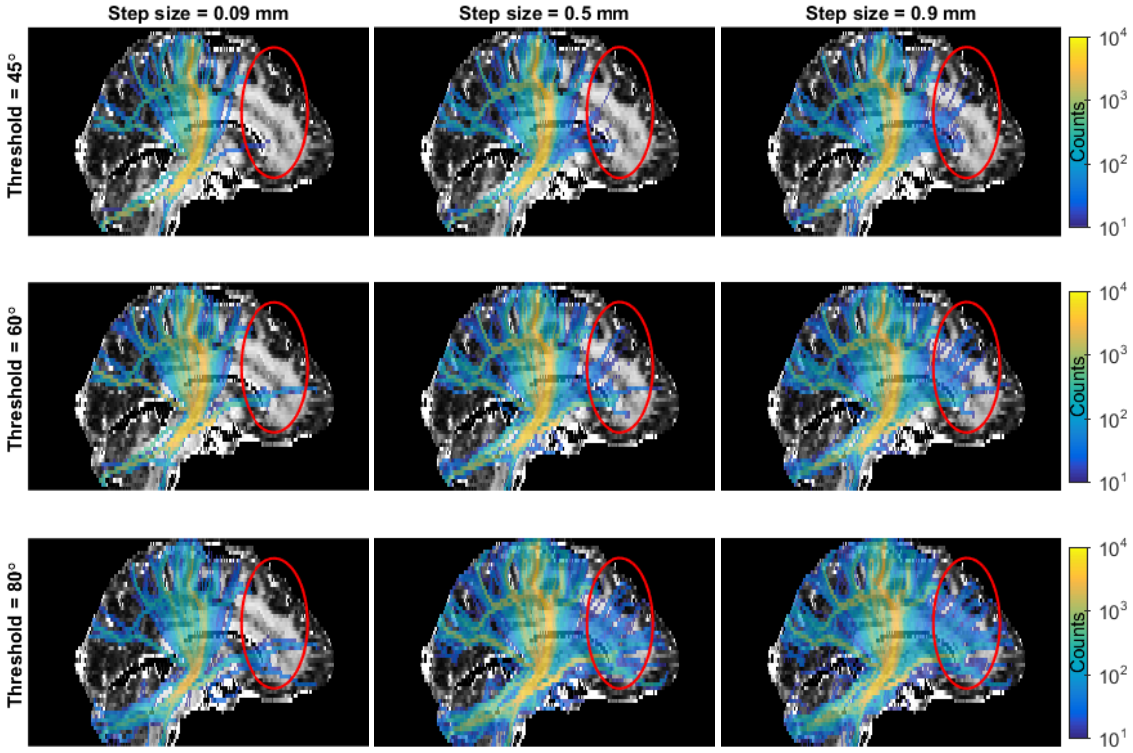

Figure 4.11: Maximum intensity projection of the streamline density in the sagittal plane for different step sizes and curvature thresholds. The streamlines are overlaid on a sagittal slice of a fractional anisotropy map. The red ellipse marks the areas most affected by the step size and curvature threshold change.

4.3. Benchmarking

4.3.1. Fibercup phantom

The results for the global tractometer measures are shown in Table 4.5. The table shows that our method had a lower median angular error than Camino. The average bundle coverage of Camino was slightly higher but simultaneously the no bundle coverage of Camino was markedly higher than our method for all noise levels.

Table 4.5: Results for the median angular error, average bundle coverage and no bundle coverage for the baseline (BL) and different noise levels (N1, N2) of the fibercup phantom.

	Median angular error			Average bundle coverage			No bundle coverage		
	BL	N1	N2	BL	N1	N2	BL	N1	N2
Our method	0.73^o	1.6^o	2.8^o	87.0%	84.4%	83.2%	10.0%	12.7%	15.0%
Camino	2.7^o	2.7^o	4.2^o	95.3%	88.7%	90.4%	47.7%	27.5%	32.0%

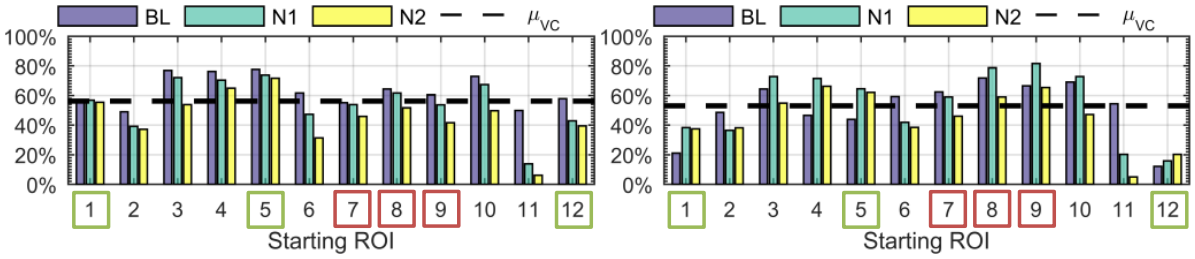

(a) Our method **(VC)**

(b) Camino **(VC)**

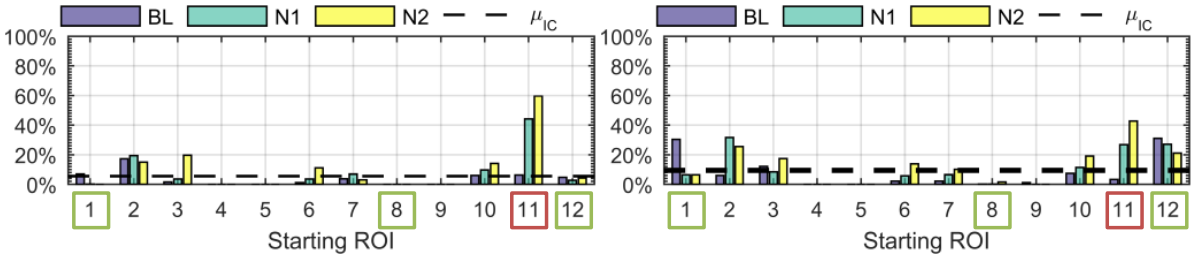

(c) Our method **(IC)**

(d) Camino **(IC)**

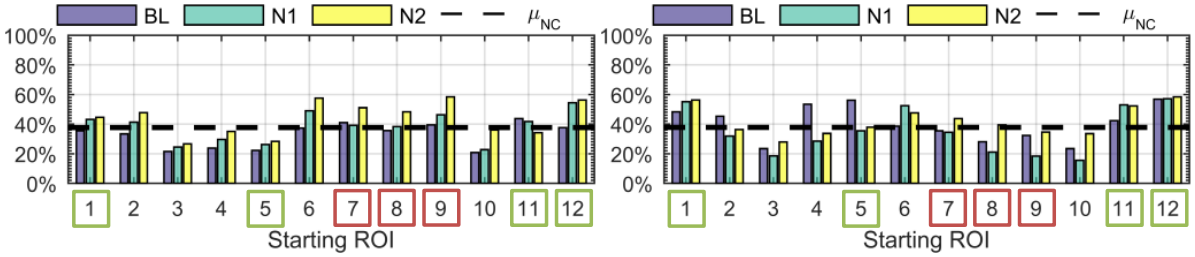

(e) Our method **(NC)**

(f) Camino **(NC)**

Figure 4.12: The percentage of valid connections (a,b), invalid connections (c,d) and no connections (e,f) per seed region for the baseline (BL) and different noise levels (N1,N2,) of the fibercup phantom. The dashed lines represent the average percentage of connections for all ROIs. The green and red squares indicate the ROIs where either our method or Camino performs better, respectively.

Figure 4.12 shows that on average the percentage of valid connections decreased for increasing noise levels, whilst the percentage of invalid and no connections increased. We used a Wilcoxon rank sum test to test whether the perceived difference in the connection types between the two methods was significant. The results are shown in Table 4.6. This table demonstrates that the two methods differed most significantly in terms of valid and no connection percentage. Importantly, our method performed better in ROIs with curved and kissing fibers (ROI 1, 5 and 12), whereas Camino performed better in ROIs with a long straight section (ROI 7, 8 and 9). Both methods seem to perform similarly in the ROIs with crossing fibers.

Table 4.6: P-values for the ROIs where the difference in performance of both methods is statistically significant.

	Our method better					Camino better			
ROI	1	5	8	11	12	7	8	9	11
Valid connections	$6.4{\cdot}10^{-9}$	$6.4{\cdot}10^{-9}$	x	x	$6.4{\cdot}10^{-9}$	0.017	0.0043	$6.4{\cdot}10^{-9}$	x
Invalid connections	0.0043	x	$6.4{\cdot}10^{-9}$	x	$6.4{\cdot}10^{-9}$	x	x	x	0.0043
No connections	$6.4{\cdot}10^{-9}$	$6.4{\cdot}10^{-9}$	x	$5.6{\cdot}10^{-5}$	$6.4{\cdot}10^{-9}$	0.0043	0.0043	$6.4{\cdot}10^{-9}$	x

4.3.2. Human data

An example of the crossing of the CC and CST streamlines is shown in Figure 4.13. There seemed to be more streamlines from the CC that crossed over the CST estimated by our algorithm than by the Camino algorithm. We have quantified this by determining the average number of streamlines passing through the fiber crossing. The results are shown in Table 4.7.

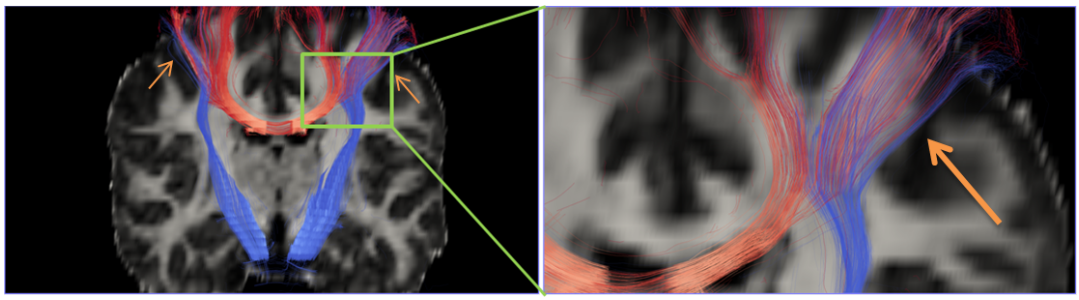

(a) Our method

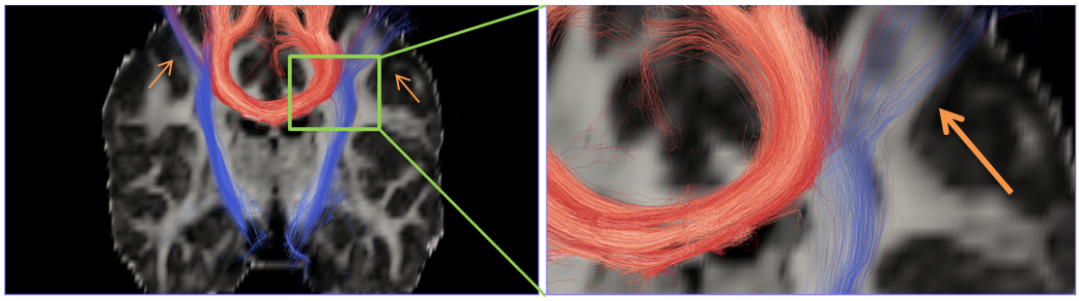

(b) Camino

Figure 4.13: Tractography outputs for the CC seed region (Red) and the CST seed region (Blue) in a coronal slice, overlaid with a fractional anisotropy map. The orange arrows indicate the crossing fibers we are interested in.

Table 4.7: The average streamline count from the CC passing the crossing with the CST

	Control 1	Control 2	Control 3	Control 4	Control 5
Our method	37	30	123	41	358
Camino	31	17	66	27	278

4.4. Application to EEG

The distribution of the dipoles over the Brodmann areas is shown in Figure 4.14. This figure shows that the sum of all the dipoles in the control group (72 dipoles) was larger than in the patient group (56 dipoles). Furhermore, most dipoles were located in the premotor-cortex for both subject-groups, because our EEG recordings were performed during wrist manipulation tasks. However, compared to the patient group, the control group showed almost double the amount of dipoles (15 vs 8) in this region.

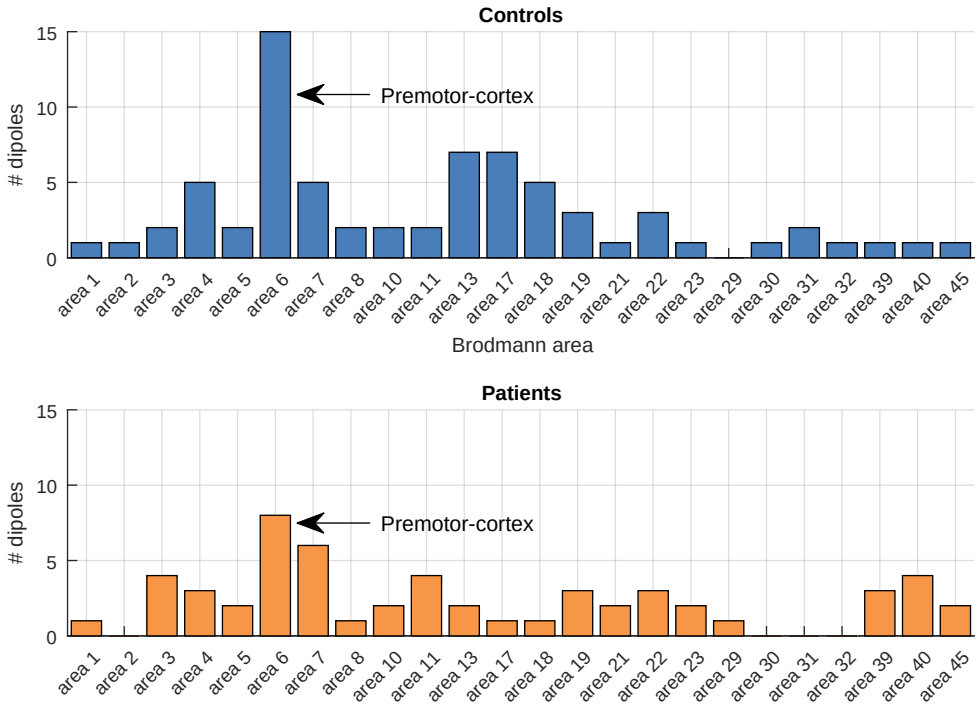

Figure 4.14: Distribution of the dipoles over the different Brodmann areas for the control and patient group.

Figure 4.15 shows that the modular structure was different in the patient group compared to the control group. Specifically, we found 7 modules in the control group, whereas 6 modules were found in the patient group. In Figure 4.15(a), the red brain region encircled by the red ellipse was formed by the sensorimotor area, which was separate from the green region formed by the primary motor cortex. However, these two regions merged together into one larger region in the patients, as can be seen in Figure 4.15(b).

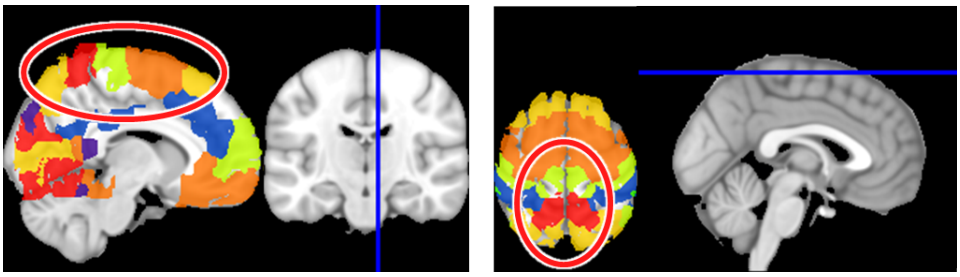

(a) Controls

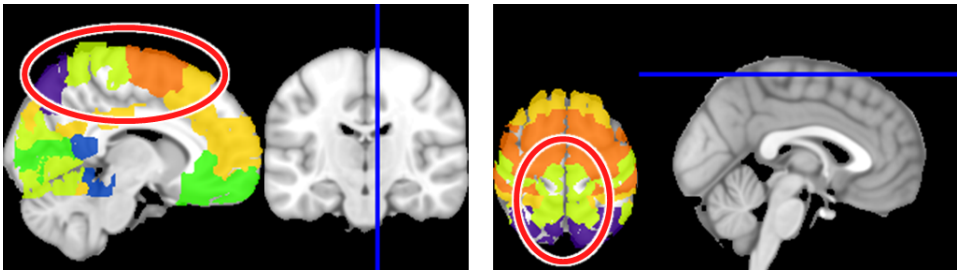

(b) Patients

Figure 4.15: The modular structure for (a) the group of controls and (b) the group of patients where each color represents a different module. Notably, similar colors across (a) and (b) do not necessarily relate to modules with similar anatomical connections or structure. The modules are overlayed on slices of the MNI-152 T1-weighted template image. The red ellipses indicate an ROI where brain regions of the patients and controls were grouped differently.

5

Discussion

5.1. Model selection validation

5.1.1. B-values

Our model selection managed to reconstruct all the fiber crossings in the fibercup phantom for one 1 out of 4 combinations of b-values. Compared to the other combinations this successful b-value combination lacked the b = 650 s/mm^2 acquisition. Essentially, this low b-value led to a worse fit of the multi-fiber compartment models on the higher b-values, as the low b-value signal lacked information about the crossing fibers. In other words, no indents were present in the signal (See Figure 4.1), which led to a similar goodness of fit for both the single and multi-fiber compartment models. Hence, our model selection selected the less complex single fiber compartment models.

Outside of the crossing, our model selection method also selected different models for the b-value combination of b = 1500 and 2000 s/mm^2 compared to the other b-value combinations. In particular, a model without an isotropic compartment was selected within the white matter bundles, which was to be expected considering that the fiber density was the highest in these bundles. In the other b-value combinations, a model with an isotropic compartment was selected and used as a compensation factor which allowed for a reasonable fit on both the low and high b-value.

5.1.2. Parametrization

Our model selection outputted comparable models for both the parametrization of the eigenvectors in spherical coordinates (Our parametrization) and in yaw, roll and pitch (The original parametrization). However, different models were selected in parts of the white matted bundles, due to a slight increase of the complexity measure when using the original parametrization.

5.1.3. Noise

The addition of noise resulted the selection of different models both in the bundles and crossings (Figure 4.4. Particularly, the introduction of noise caused the log likelihoods (Our measure for goodness of fit) of the model fits to converge to similar values. Consequently, less complex single fiber-compartment models were selected in the fiber crossings when noise was increased.

5.1.4. In-vivo

In-vivo, our model selection produced outputs that were in accordance with expectations, as multi-fiber compartment models were selected in the fiber crossing formed by bundles coming from the corpus callosum and the corticospinal tract (Figure 4.5). Furthermore, the combination of the lower b-value of 1000 s/mm^2 and the b-value of 2000 s/mm^2 proved to be sufficient to capture the complex fiber configurations. Importantly, this gives us an indication of the lower bound for the b-value that still allows for the reconstruction of crossing fibers, as we found that including a slightly lower b-value of 650 s/mm^2 hindered this reconstruction.

5.2. Sensitivity analysis

5.2.1. Step size

The sensitivity analysis on the step size showed that an increase in step size influenced the amount of valid connections and no connections, and the angular error (Figure 4.6(a,b,d)). Specifically, an increase in step size caused a decrease in valid connection percentage and an increase in no connection percentage, which can be explained by a higher sensitivity of the tractography to the uncertainty in fiber orientation for increasing step size [86]. Generally, voxels with a higher uncertainty have a higher probability for sampling a fiber orientation that deviates from the true fiber orientation. In the case of a small step size, the effect of these extreme orientations is averaged out, as multiple steps are taken within one voxel. However, this averaging effect does not take place for a large step size with only one step per voxel, thus more erroneous streamlines are produced.

For larger step sizes, the tractography also suffered more from overshooting curves in strongly curved bundles, such as around ROI 1, 2, 4 and 5 (see Figure 3.2(a)), which led to an increase in the amount of no connections. Additionally, we found an increase of the angular error with increasing step size, which could be attributed to the averaging effect of smaller step sizes.

The amount of invalid connections was not found to be influenced significantly by an increase in step size (Figure 4.6(c) and Table 4.3 / 4.4), while we would expect more invalid connections as the larger step sizes are more likely to deviate from the true fiber orientation. However, this effect was most likely counteracted by the increase in no connections which results in less streamlines actually reaching another ROI.

In Table 4.3 and 4.4, we could see that a smaller step size related to a better performance in terms of valid connection and no connection. However, no significant difference was found between the step sizes of 0.25 and 0.5 mm. In a practical situation it would be preferable to then choose the larger step size, as a doubling of the step size will lead to half as many steps per streamline and, consequently, less calculation time. Moreover, the averaging effect of the smaller step size would lead to an underestimation of the true fiber distribution which is undesirable [86].

With respect to the bundle coverage, the step size was found to mainly influence the no bundle coverage, which increased slightly with increasing step size. This could be attributed to the aforementioned sensitivity to uncertainty, which leads to more visits to voxels that are not related to the target bundle. The average bundle coverage was not influenced by the step size, which means that our tractography algorithm still produced streamlines that propagate in the target bundle even though the amount of valid connections decreased when increasing the step size.

5.2.2. Curvature threshold

The influence of the curvature threshold was found to be smaller than that of the step size. The main parameters influenced by the curvature threshold were the amount of invalid connections and the no bundle coverage. Overall, the effect of the lowering the curvature threshold was a decrease in streamlines that deviate from the underlying fiber orientations, which explains the decrease in both invalid connections and no bundle coverage.

5.2.3. In-vivo

Lastly, the in-vivo results seemed to follow a slightly different pattern than that of the fibercup phantom. Particularly, we noted a larger effect of the curvature threshold in-vivo. Most likely, this difference was caused by the constraints put on the tractography in the fibercup phantom, which limits the tractography to the white matter bundles. In-vivo, such a limitation was not applied, as no ground truth exists for the complex configurations of the white matter bundles in the brain.

5.2.4. Relevance for our tractography

The sensitivity analysis on the fibercup phantom seemed to indicate that a smaller step size would lead to a better tractography outcome. Specifically, the smaller step size effectively makes the tractography behave more deterministic, due to the averaging effect that was mentioned before. In the fibercup phantom, this more deterministic behavior led to better results due to the relatively simple white matter configurations modeled by this phantom. However, our aim was to develop a probabilistic tractography algorithm, which means that larger step sizes are needed.

In vivo, the use of a large step size and curvature thresholds caused the streamlines to go into more parts of the brain. However, the results on the fibercup phantom showed that such a large step size led to a higher

number of erroneously reconstructed bundles. Therefore, an intermediate step size (Around 0.5 mm for our in-vivo data) should be used in practice, as this would make our tractography behave in a probabilistic way while also being less sensitive to outliers in the sampling. Furthermore, the in-vivo results showed that using such a step size combined with a high curvature threshold (80°) would allow for streamlines to enter deeper into the gray matter, which is where the dipoles from our EEG data are located.

5.3. Benchmarking

5.3.1. Fibercup

In the benchmarking results, the global tractometer measures showed that the median angular error for our method was consistently lower than that of Camino. This could be attributed to the different methods used for estimating the fiber uncertainty. Notably, the fiber orientation PDFs in Camino are based on the link between the relative magnitude and orientations of the DT's second and third eigenvectors and the uncertainty in fiber orientation [58]. This shape of the tensor might be invariant at lower noises levels, therefore introducing a higher angular error. Our method derives the uncertainty from the CRLB, whose value decreases with lower noise levels [75]. The higher uncertainty in fiber orientation in Camino also explains the higher average bundle coverage, as it allows the tractography to explore more voxels. However, this also leads to a higher no bundle coverage which is undesirable.

The ROI specific tractometer measures showed that both methods differed most significantly in terms of their performance on curved (Our method better) and straight bundles (Camino better). In practice, curved bundles are more likely to be found in the brain than long straight bundles. Therefore, we expect that our method would be better suited for applications in human data than Camino.

The observed decrease in valid connections with noise level, especially the one in ROI 11 (see 4.12), was due to not discerning the fiber crossing by both our method and Camino's. In the case of Camino, which selects models based on fitted diffusion type (e.g. Non-Gaussian or Gaussian diffusion), the diffusion in the crossing is considered to be merely Gaussian [52]. The erroneous classification in our model selection stems from the effect of noise on the log likelihood of the different model fits. This log likelihood converges to similar values for all models, effectively causing our model selection to pick the simplest (Gaussian) model.

5.3.2. Human data

As our method was applied to human data more fibers were tracked across the fiber crossing than with Camino. In this region we observed that the magnitude of the second eigenvector was similar to that of the first eigenvector. In Camino this leads to an increased uncertainty, hence, fewer fibers passing the crossing. Performance of our method was not reduced as the uncertainty is based on the noise level and not tensor shape.

5.4. Limitations

There are two limitations to the use of our method for probabilistic tractography. First of all, the data needs to have multiple b-values, which preferably consist of a low b-value of at least 1000 $mm^2\ s^{-1}$ and a high b-value of about 2000 $mm^2\ s^{-1}$. This is necessary to fit the more complex dual tensor models [24]. Secondly, there is the influence of noise on the model selection. This limitation was observed in a crossing with lower diffusivity in the fibercup phantom and resulted in selection of single tensor models. Still, the performance on the human data, which is comparable in SNR to most modern dMRI acquisitions, suggests that tracking across in-vivo crossings is very well possible.

5.5. Application to EEG

In the application of our framework to EEG data, the control group had more dipoles in the premotor cortex than the patient group. This premotor cortex plays a role in voluntary movements. [11]. Notably, all the patients had a stroke which affected their motor function. Therefore, connections to the premotor cortex might be affected, which might lead to less activity (fewer dipoles) in this region during the wrist task in the patient group.

Our investigation of the connectivity showed a different modular structure in the patient group compared to the control group, as the same number of Brodmann areas was divided up into fewer modules in the patient group. Furthermore, the sensorimotor area and the primary motor cortex were assigned to the same module in the patient group, while they were in separate modules in the control group. Possibly, the merging of these

modules points towards more integration of the sensorimotor cortex and primary motor cortex in the stroke patients, which might be related to the role of the sensory pathways in stroke recovery found in literature. In research by Vlaar et al. [5], the integrity of these sensory pathways was found to correlate with motor recovery after stroke.

6

Conclusion and recommendations

In this thesis, we presented a framework for model selection and probabilistic tractography. Specifically, our framework provides a method for parsimonious model selection in the form of the ICOMP-TKLD criterion and uses the Cramér-Rao lower bound to capture the uncertainty in the estimated fiber orientations.

The performance of our method was assessed using both the fibercup phantom and human data. We have shown that our model selection method can reconstruct fiber crossing at noise levels and b-values comparable to clinical acquisitions, which has been verified on the data from 7 healthy controls. Furthermore, we have investigated the sensitivity of our tractography to changes in both step size and curvature threshold. In general, a smaller step size and lower curvature thresholds resulted in more deterministic behavior, while a larger step sizes and higher curvature thresholds led to more probabilistic behavior and deeper propagation into the gray matter in human data. However, a too large step size, in the order of the voxel size (~0.9 to 3 mm), should be avoided, as this leads to more erroneously reconstructed bundles due to a higher sensitivity to outliers. In practice, an intermediate steps size of 0.5 mm and a curvature threshold of 80° should be used on our data, as this allows for a probabilistic tractography while reducing the effect of outliers.

Our comparison with the open source dMRI toolkit Camino [10] showed that on the fibercup phantom our method performs either better or similarly to Camino software. Furthermore, a comparison on human data showed that our method performs better at following curved bundles, and at tracking across the crossing of the corpus callosum and corticospinal tract.

All in all, our results both on the fibercup phantom and especially on the human data suggest that sophisticated diffusion tensor reconstruction techniques combined with model selection procedures can lead to improved fiber tractography outcomes. Furthermore, the results indicate that it is feasible to use our model selection method to reconstruct fiber crossings and the Cramér-Rao lower bound as a measure of uncertainty in probabilistic tractography. Lastly, the ability of our framework to track into the gray matter and across fiber crossings makes it a suitable tool to track from source locations found in EEG.

6.1. Recommendations

A few recommendations can be done for future work. First of all, the performance of our model selection method on the fibercup phantom suggests that for reconstructing a fiber crossing, a combination with an intermediate (1500 s/mm) and a (2000 s/mm) high b-value works better than one with a high and a low (650 s/mm) b-value. However, our human data did not have such an intermediate b-value. Therefore, it would be interesting investigate if the same principle holds in human data or if this benefit is negated by the decreased signal-to-noise ratio of the intermediate b-value.

The output of the tractography would be another interesting aspect to investigate. Specifically, the streamline count which quantify the probability of connection. These streamline counts have somewhat of a distance bias, as there is a higher density of streamlines closer to the seed point [23]. In general, prior knowledge about the brain anatomy is necessary to extract regions that both have high streamline counts and are anatomically plausible. Therefore, it would be useful to have a connectivity atlas. This connectivity atlas would take the streamlines generated by the tractography as input, and automatically highlight regions that have a high connection probability (streamline count) and are anatomically plausible.

Bibliography

[1] Valery L Feigin, Mohammad H Forouzanfar, Rita Krishnamurthi, George A Mensah, Myles Connor, Derrick A Bennett, Andrew E Moran, Ralph L Sacco, Laurie Anderson, Thomas Truelsen, et al. Global and regional burden of stroke during 1990–2010: findings from the global burden of disease study 2010. *The Lancet*, 383(9913):245–255, 2014.

[2] Valery L Feigin, Carlene MM Lawes, Derrick A Bennett, Suzanne L Barker-Collo, and Varsha Parag. Worldwide stroke incidence and early case fatality reported in 56 population-based studies: a systematic review. *The Lancet Neurology*, 8(4):355–369, 2009.

[3] Winston D Byblow, Cathy M Stinear, P Alan Barber, Matthew A Petoe, and Suzanne J Ackerley. Proportional recovery after stroke depends on corticomotor integrity. *Annals of neurology*, 78(6):848–859, 2015.

[4] Philipp Koch, Robert Schulz, and Friedhelm C Hummel. Structural connectivity analyses in motor recovery research after stroke. *Annals of clinical and translational neurology*, 3(3):233–244, 2016.

[5] Martijn P Vlaar, Teodoro Solis-Escalante, Julius PA Dewald, Erwin EH van Wegen, Alfred C Schouten, Gert Kwakkel, and Frans CT van der Helm. Quantification of task-dependent cortical activation evoked by robotic continuous wrist joint manipulation in chronic hemiparetic stroke. *Journal of neuroengineering and rehabilitation*, 14(1):30, 2017.

[6] Peter J Basser, James Mattiello, and Denis LeBihan. Mr diffusion tensor spectroscopy and imaging. *Biophysical journal*, 66(1):259–267, 1994.

[7] Daniel C Alexander, Penny L Hubbard, Matt G Hall, Elizabeth A Moore, Maurice Ptito, Geoff JM Parker, and Tim B Dyrby. Orientationally invariant indices of axon diameter and density from diffusion mri. *Neuroimage*, 52(4):1374–1389, 2010.

[8] Timothy EJ Behrens, MW Woolrich, Mark Jenkinson, H Johansen-Berg, RG Nunes, S Clare, PM Matthews, J Michael Brady, and Stephen M Smith. Characterization and propagation of uncertainty in diffusion-weighted mr imaging. *Magnetic resonance in medicine*, 50(5):1077–1088, 2003.

[9] Timothy EJ Behrens, H Johansen Berg, Saad Jbabdi, MFS Rushworth, and MW Woolrich. Probabilistic diffusion tractography with multiple fibre orientations: What can we gain? *Neuroimage*, 34(1):144–155, 2007.

[10] PA Cook, Y Bai, SKKS Nedjati-Gilani, KK Seunarine, MG Hall, GJ Parker, and DC Alexander. Camino: open-source diffusion-mri reconstruction and processing. In *14th scientific meeting of the international society for magnetic resonance in medicine*, volume 2759. Seattle WA, USA, 2006.

[11] EN Marieb and K Hoehn. *Human Anatomy and Physiology*. Pearson, 9 edition, 2009.

[12] Ischemic stroke. `https://neurosciences.uvahealth.com/services/stroke-center/stroke`. Accessed: 03-07-2017.

[13] Deborah S Nichols-Larsen, PC Clark, Angelique Zeringue, Arlene Greenspan, and Sarah Blanton. Factors influencing stroke survivors' quality of life during subacute recovery. *Stroke*, 36(7):1480–1484, 2005.

[14] Floor Buma, Gert Kwakkel, and Nick Ramsey. Understanding upper limb recovery after stroke. *Restorative neurology and neuroscience*, 31(6):707–722, 2013.

[15] Susumu Mori and Peter B Barker. Diffusion magnetic resonance imaging: its principle and applications. *The Anatomical Record*, 257(3):102–109, 1999.

[16] Christian Beaulieu. The basis of anisotropic water diffusion in the nervous system–a technical review. *NMR in Biomedicine*, 15(7-8):435–455, 2002.

[17] Robert W Brown, Y-C Norman Cheng, E Mark Haacke, Michael R Thompson, and Ramesh Venkatesan. *Magnetic resonance imaging: physical principles and sequence design*. John Wiley & Sons, 2014.

[18] Herman Y Carr and Edward M Purcell. Effects of diffusion on free precession in nuclear magnetic resonance experiments. *Physical review*, 94(3):630, 1954.

[19] Edward O Stejskal and John E Tanner. Spin diffusion measurements: spin echoes in the presence of a time-dependent field gradient. *The journal of chemical physics*, 42(1):288–292, 1965.

[20] Denis Le Bihan, Jean-François Mangin, Cyril Poupon, Chris A Clark, Sabina Pappata, Nicolas Molko, and Hughes Chabriat. Diffusion tensor imaging: concepts and applications. *Journal of magnetic resonance imaging*, 13(4):534–546, 2001.

[21] Denis Le Bihan, Cyril Poupon, Alexis Amadon, and Franck Lethimonnier. Artifacts and pitfalls in diffusion mri. *Journal of magnetic resonance imaging*, 24(3):478–488, 2006.

[22] Mara Cercignani and Mark A Horsfield. The physical basis of diffusion-weighted mri. *Journal of the neurological sciences*, 186:S11–S14, 2001.

[23] Jacques-Donald Tournier, Susumu Mori, and Alexander Leemans. Diffusion tensor imaging and beyond. *Magnetic resonance in medicine*, 65(6):1532–1556, 2011.

[24] Matthan WA Caan, H Ganesh Khedoe, Dirk HJ Poot, J Arjan, Silvia D Olabarriaga, Kees A Grimbergen, Lucas J Van Vliet, and Frans M Vos. Estimation of diffusion properties in crossing fiber bundles. *IEEE transactions on medical imaging*, 29(8):1504–1515, 2010.

[25] Peter J Basser and Derek K Jones. Diffusion-tensor mri: theory, experimental design and data analysis–a technical review. *NMR in Biomedicine*, 15(7-8):456–467, 2002.

[26] Peter J Basser, James Mattiello, and Denis LeBihan. Estimation of the effective self-diffusion tensor from the nmr spin echo. *Journal of Magnetic Resonance, Series B*, 103(3):247–254, 1994.

[27] P Mukherjee, JI Berman, SW Chung, CP Hess, and RG Henry. Diffusion tensor mr imaging and fiber tractography: theoretic underpinnings. *American journal of neuroradiology*, 29(4):632–641, 2008.

[28] Niels Buchmann, Jens Gempt, Michael Stoffel, Annette Foerschler, Bernhard Meyer, and Florian Ringel. Utility of diffusion tensor-imaged (dti) motor fiber tracking for the resection of intracranial tumors near the corticospinal tract. *Acta neurochirurgica*, 153(1):68–74, 2011.

[29] Takeshi Imura, Yuki Nagasawa, Tetsuji Inagawa, Naoki Imada, Hiroaki Izumi, Katsuya Emoto, Itaru Tani, Hiroyuki Yamasaki, Yuichiro Ota, Shuichi Oki, et al. Prediction of motor outcomes and activities of daily living function using diffusion tensor tractography in acute hemiparetic stroke patients. *Journal of physical therapy science*, 27(5):1383–1386, 2015.

[30] Derek K Jones, Thomas R Knösche, and Robert Turner. White matter integrity, fiber count, and other fallacies: the do's and don'ts of diffusion mri. *Neuroimage*, 73:239–254, 2013.

[31] Alexander Lerner, Monique A Mogensen, Paul E Kim, Mark S Shiroishi, Darryl H Hwang, and Meng Law. Clinical applications of diffusion tensor imaging. *World neurosurgery*, 82(1):96–109, 2014.

[32] Terry A Gaige, Thomas Benner, Ruopeng Wang, Van J Wedeen, and Richard J Gilbert. Three dimensional myoarchitecture of the human tongue determined in vivo by diffusion tensor imaging with tractography. *Journal of Magnetic Resonance Imaging*, 26(3):654–661, 2007.

[33] Christina Tsien, Yue Cao, and Thomas Chenevert. Clinical applications for diffusion magnetic resonance imaging in radiotherapy. In *Seminars in radiation oncology*, volume 24, pages 218–226. Elsevier, 2014.

[34] David S Tuch, Timothy G Reese, Mette R Wiegell, Nikos Makris, John W Belliveau, and Van J Wedeen. High angular resolution diffusion imaging reveals intravoxel white matter fiber heterogeneity. *Magnetic resonance in medicine*, 48(4):577–582, 2002.

[35] Ben Jeurissen, Alexander Leemans, Jacques-Donald Tournier, Derek K Jones, and Jan Sijbers. Investigating the prevalence of complex fiber configurations in white matter tissue with diffusion magnetic resonance imaging. *Human brain mapping*, 34(11):2747–2766, 2013.

[36] Shawna Farquharson, J-Donald Tournier, Fernando Calamante, Gavin Fabinyi, Michal Schneider-Kolsky, Graeme D Jackson, and Alan Connelly. White matter fiber tractography: why we need to move beyond dti: Clinical article. *Journal of neurosurgery*, 118(6):1367–1377, 2013.

[37] Ben Jeurissen, Alexander Leemans, Derek K Jones, Jacques-Donald Tournier, and Jan Sijbers. Probabilistic fiber tracking using the residual bootstrap with constrained spherical deconvolution. *Human brain mapping*, 32(3):461–479, 2011.

[38] Kathleen M Curran, Louise Emsell, and Alexander Leemans. Quantitative dti measures. In *Diffusion Tensor Imaging*, pages 65–87. Springer, 2016.

[39] Van J Wedeen, Patric Hagmann, Wen-Yih Isaac Tseng, Timothy G Reese, and Robert M Weisskoff. Mapping complex tissue architecture with diffusion spectrum magnetic resonance imaging. *Magnetic resonance in medicine*, 54(6):1377–1386, 2005.

[40] David S Tuch. Q-ball imaging. *Magnetic resonance in medicine*, 52(6):1358–1372, 2004.

[41] Kalvis M Jansons and Daniel C Alexander. Persistent angular structure: new insights from diffusion magnetic resonance imaging data. *Inverse problems*, 19(5):1031, 2003.

[42] Yaniv Assaf, Raisa Z Freidlin, Gustavo K Rohde, and Peter J Basser. New modeling and experimental framework to characterize hindered and restricted water diffusion in brain white matter. *Magnetic Resonance in Medicine*, 52(5):965–978, 2004.

[43] BW Kreher, JF Schneider, I Mader, E Martin, J Hennig, and KA Il'Yasov. Multitensor approach for analysis and tracking of complex fiber configurations. *Magnetic resonance in medicine*, 54(5):1216–1225, 2005.

[44] Yaniv Assaf and Peter J Basser. Composite hindered and restricted model of diffusion (charmed) mr imaging of the human brain. *Neuroimage*, 27(1):48–58, 2005.

[45] Hui Zhang, Torben Schneider, Claudia A Wheeler-Kingshott, and Daniel C Alexander. Noddi: practical in vivo neurite orientation dispersion and density imaging of the human brain. *Neuroimage*, 61(4):1000–1016, 2012.

[46] David E Sosnovik, Ruopeng Wang, Guangping Dai, Timothy G Reese, and Van J Wedeen. Diffusion mr tractography of the heart. *Journal of Cardiovascular Magnetic Resonance*, 11(1):47, 2009.

[47] Tim P Hosey, Sally G Harding, T Adrian Carpenter, Richard E Ansorge, and Guy B Williams. Application of a probabilistic double-fibre structure model to diffusion-weighted mr images of the human brain. *Magnetic resonance imaging*, 26(2):236–245, 2008.

[48] J-Donald Tournier, Fernando Calamante, David G Gadian, and Alan Connelly. Direct estimation of the fiber orientation density function from diffusion-weighted mri data using spherical deconvolution. *NeuroImage*, 23(3):1176–1185, 2004.

[49] Nicolas Kunz, Hui Zhang, Lana Vasung, Kieran R O'brien, Yaniv Assaf, François Lazeyras, Daniel C Alexander, and Petra S Hüppi. Assessing white matter microstructure of the newborn with multi-shell diffusion mri and biophysical compartment models. *Neuroimage*, 96:288–299, 2014.

[50] Flavio Dell'Acqua, Andrew Simmons, Steven CR Williams, and Marco Catani. Can spherical deconvolution provide more information than fiber orientations? hindrance modulated orientational anisotropy, a true-tract specific index to characterize white matter diffusion. *Human brain mapping*, 34(10):2464–2483, 2013.

[51] Saad Jbabdi, Stamatios N Sotiropoulos, Alexander M Savio, Manuel Graña, and Timothy EJ Behrens. Model-based analysis of multishell diffusion mr data for tractography: How to get over fitting problems. *Magnetic Resonance in Medicine*, 68(6):1846–1855, 2012.

[52] DC Alexander, GJ Barker, and SR Arridge. Detection and modeling of non-gaussian apparent diffusion coefficient profiles in human brain data. *Magnetic Resonance in Medicine*, 48(2):331–340, 2002.

[53] Raisa Z Freidlin, Evren Ozarslan, Michal E Komlosh, Lin-Ching Chang, Cheng Guan Koay, Derek K Jones, and Peter J Basser. Parsimonious model selection for tissue segmentation and classification applications: a study using simulated and experimental dti data. *IEEE transactions on medical imaging*, 26(11):1576–1584, 2007.

[54] J-F Mangin, Pierre Fillard, Yann Cointepas, Denis Le Bihan, Vincent Frouin, and Cyril Poupon. Toward global tractography. *NeuroImage*, 80:290–296, 2013.

[55] Daan Christiaens, Marco Reisert, Thijs Dhollander, Stefan Sunaert, Paul Suetens, and Frederik Maes. Global tractography of multi-shell diffusion-weighted imaging data using a multi-tissue model. *NeuroImage*, 123:89–101, 2015.

[56] Susumu Mori and Peter van Zijl. Fiber tracking: principles and strategies–a technical review. *NMR in Biomedicine*, 15(7-8):468–480, 2002.

[57] Derek K Jones. Determining and visualizing uncertainty in estimates of fiber orientation from diffusion tensor mri. *Magnetic Resonance in Medicine*, 49(1):7–12, 2003.

[58] Geoffrey JM Parker, Hamied A Haroon, and Claudia AM Wheeler-Kingshott. A framework for a streamline-based probabilistic index of connectivity (pico) using a structural interpretation of mri diffusion measurements. *Journal of Magnetic Resonance Imaging*, 18(2):242–254, 2003.

[59] Derek K Jones. Tractography gone wild: probabilistic fibre tracking using the wild bootstrap with diffusion tensor mri. *IEEE transactions on medical imaging*, 27(9):1268–1274, 2008.

[60] H-W Chung, M-C Chou, and C-Y Chen. Principles and limitations of computational algorithms in clinical diffusion tensor mr tractography. *American Journal of Neuroradiology*, 32(1):3–13, 2011.

[61] Jianfei Yang, Dirk HJ Poot, Matthan WA Caan, Tanja Su, Charles BLM Majoie, Lucas J van Vliet, and Frans M Vos. Reliable dual tensor model estimation in single and crossing fibers based on jeffreys prior. *PloS one*, 11(10):e0164336, 2016.

[62] Peter J Basser, Sinisa Pajevic, Carlo Pierpaoli, Jeffrey Duda, and Akram Aldroubi. In vivo fiber tractography using dt-mri data. *Magnetic resonance in medicine*, 44(4):625–632, 2000.

[63] Tim B Dyrby, Lise V Søgaard, Geoffrey J Parker, Daniel C Alexander, Nanna M Lind, William FC Baaré, Anders Hay-Schmidt, Nina Eriksen, Bente Pakkenberg, Olaf B Paulson, et al. Validation of in vitro probabilistic tractography. *Neuroimage*, 37(4):1267–1277, 2007.

[64] Jennifer SW Campbell and G Bruce Pike. Potential and limitations of diffusion mri tractography for the study of language. *Brain and language*, 131:65–73, 2014.

[65] Jeremy C Lim, Pramit M Phal, Patricia M Desmond, Andrew D Nichols, Chris Kokkinos, Helen V Danesh-Meyer, Andrew H Kaye, and Bradford A Moffat. Probabilistic mri tractography of the optic radiation using constrained spherical deconvolution: a feasibility study. *PloS one*, 10(3):e0118948, 2015.

[66] Khalid Hamandi, HW Robert Powell, Helmut Laufs, Mark R Symms, Gareth J Barker, Geoff JM Parker, Louis Lemieux, and JS Duncan. Combined eeg-fmri and tractography to visualise propagation of epileptic activity. *Journal of Neurology, Neurosurgery & Psychiatry*, 79(5):594–597, 2008.

[67] Faiza Javad, Jason D Warren, Caroline Micallef, John S Thornton, Xavier Golay, Tarek Yousry, and Laura Mancini. Auditory tracts identified with combined fmri and diffusion tractography. *Neuroimage*, 84:562–574, 2014.

[68] Catherine Jean Chu, Naoaki Tanaka, J Diaz, Brian L Edlow, Ona Wu, M Hämäläinen, S Stufflebeam, Sydney S Cash, and Mark A Kramer. Eeg functional connectivity is partially predicted by underlying white matter connectivity. *Neuroimage*, 108:23–33, 2015.

[69] Thomas Schultz, Anna Vilanova, Ralph Brecheisen, and Gordon Kindlmann. Fuzzy fibers: Uncertainty in dmri tractography. In *Scientific Visualization*, pages 79–92. Springer, 2014.

[70] Thomas Koenig. Basic principles of eeg and meg analysis. 2014.

[71] Mayuresh Sudhakar Korgaonkar. *Development of a multi-modal neuroimaging fusion approach to study rehabilitation of aphasia stroke patients*. State University of New York at Stony Brook, 2008.

[72] Scott Makeig, Anthony J Bell, Tzyy-Ping Jung, and Terrence J Sejnowski. Independent component analysis of electroencephalographic data. In *Advances in neural information processing systems*, pages 145–151, 1996.

[73] Dietrich Lehmann. Brain electric microstates and cognition: the atoms of thought. In *Machinery of the Mind*, pages 209–224. Springer, 1990.

[74] Paula Trujillo, Alfonso Mastropietro, Alessandro Scano, Andrea Chiavenna, Simona Mrakic-Sposta, Marco Caimmi, Franco Molteni, and Giovanna Rizzo. Quantitative eeg for predicting upper-limb motor recovery in chronic stroke robot-assisted rehabilitation. *IEEE Transactions on Neural Systems and Rehabilitation Engineering*, 2017.

[75] Farid Ahmed Sid, Karim Abed-Meraim, Rachid Harba, and Fatima Oulebsir-Boumghar. Analytical performance bounds for multi-tensor diffusion-mri. *Magnetic Resonance Imaging*, 36:146–158, 2017.

[76] Dirk HJ Poot and Stefan Klein. Detecting statistically significant differences in quantitative mri experiments, applied to diffusion tensor imaging. *IEEE transactions on medical imaging*, 34(5):1164–1176, 2015.

[77] Jianfei Yang, Dirk HJ Poot, Matthan WA Caan, Frans M Vos, and Lucas J van Vliet. Rank-2 model-order selection in diffusion tensor mri: Information complexity based on the total kullback-leibler divergence. In *Biomedical Imaging (ISBI), 2015 IEEE 12th International Symposium on*, pages 926–929. IEEE, 2015.

[78] Hamparsum Bozdogan. Akaike's information criterion and recent developments in information complexity. *Journal of mathematical psychology*, 44(1):62–91, 2000.

[79] Baba C Vemuri, Meizhu Liu, Shun-Ichi Amari, and Frank Nielsen. Total bregman divergence and its applications to dti analysis. *IEEE Transactions on medical imaging*, 30(2):475–483, 2011.

[80] Jianfei Yang, Dirk HJ Poot, Lucas J Van Vliet, and Frans M Vos. Estimation of diffusion properties in three-way fiber crossings without overfitting. *Physics in medicine and biology*, 60(23):9123, 2015.

[81] Peter F Neher, Maxime Descoteaux, Jean-Christophe Houde, Bram Stieltjes, and Klaus H Maier-Hein. Strengths and weaknesses of state of the art fiber tractography pipelines–a comprehensive in-vivo and phantom evaluation study using tractometer. *Medical image analysis*, 26(1):287–305, 2015.

[82] Marc-Alexandre Côté, Gabriel Girard, Arnaud Boré, Eleftherios Garyfallidis, Jean-Christophe Houde, and Maxime Descoteaux. Tractometer: towards validation of tractography pipelines. *Medical image analysis*, 17(7):844–857, 2013.

[83] Sangma Xie, Nianming Zuo, Liqing Shang, Ming Song, Lingzhong Fan, and Tianzi Jiang. How does b-value affect hardi reconstruction using clinical diffusion mri data? *PloS one*, 10(3):e0120773, 2015.

[84] Mikail Rubinov and Olaf Sporns. Complex network measures of brain connectivity: uses and interpretations. *Neuroimage*, 52(3):1059–1069, 2010.

[85] Chris Rorden, Hans-Otto Karnath, and Leonardo Bonilha. Improving lesion-symptom mapping. *Journal of cognitive neuroscience*, 19(7):1081–1088, 2007.

[86] JD Tournier, F Calamante, A Connelly, et al. Effect of step size on probabilistic streamlines: implications for the interpretation of connectivity analysis. In *Proc Intl Soc Mag Reson Med*, volume 19, page 2019, 2011.